CHRISTINA DIMOPOULOU

UNIVERSITY OF ATHENS , PHYSICS DEPARTMENT

1997 CERN SUMMER STUDENT

NEUTRINO PHYSICS

and

DESIGN OF THE FOCUSING SYSTEM FOR THE CERN TO GRAN SASSO NEUTRINO BEAM-LINE.

ATHENS

MAY 1998

LIST OF CONTENTS

CHAPTER 3

DESIGN OF THE MAGNETIC HORN

1.General purpose and requirements.

2. Motion of a charged particle inside the magnetic field of the horn.

2.1 Equations of motion.

2.2 Approximative solutions to the equations of motion.

3. Procedure for determining the shape of the inner conductor.

3.1 Computational scheme.

3.2 An elegant approximative formula.

3.3 Examples.

CHAPTER 4

DESIGN OF THE REFLECTOR

1. Reflector required to focus particles underfocused by the horn.

2. Reflector required to focus parent particles overfocused by the horn.

3. Examples.

CHAPTER 5

CONCLUSIONS

1. Preliminary attempts to take into account the actual E and p_T distributions of the parent particles.

2. Final Remarks.

LIST OF REFERENCES

PREFACE

This thesis was based on the work I did at CERN, in 1997, as a Summer Student, concerning the design of the focusing system for the new CERN to Gran Sasso beam-line.

Chapter 1 is a survey of neutrino physics, from an experimental physicist's point of view, insisting particularly on neutrino oscillations and the relative experiments. Emphasis is given to the CERN $\nu_\mu - \nu_\tau$ oscillation programme and to the CERN to Gran Sasso neutrino beam-line, which is being planned at present.

Chapter 2 gives specific conceptual and technical information about the focusing elements (horn and reflector) of the CERN WANF.

Chapter 3 contains the theoretical calculations permitting to determine the geometry of a horn inner conductor.

Chapter 4 contains the theoretical calculations permitting to determine the geometry of a reflector inner conductor, provided that the horn is already fixed.

In chapter 5 attempts are made to design a more realistic magnetic horn by taking into account the actual energy and p_T distributions of neutrino parent particles. Some directions concerning the future work to be done to choose the appropriate focusing system are given as well.

I would like to thank my supervisor at CERN, Mr E.Tsesmelis for his precious help and his excellent collaboration as well as Mr A.Ball for his advice and encouragement.

Christina Dimopoulou

Athens, May 1998.

CHAPTER 1

SURVEY OF NEUTRINO PHYSICS

1.THEORY OF NEUTRINO OSCILLATIONS.

1.1 Neutrino oscillations in vacuum.

Pontecorvo and independently Maki have proposed the hypothesis of neutrino mixing, according to which the 3 known neutrino flavours ν_e , ν_μ and ν_τ are not mass eigenstates but superpositions of the 3 mass eigenstates ν_1 , ν_2 and ν_3. The mass eigenvalues corresponding to the eigenstates ν_1, ν_2 and ν_3 are m_1, m_2 and m_3 respectively.

$$\nu_\alpha = \sum_i U_{\alpha i}\nu_i \qquad (1)$$

where $\alpha = e,\mu,\tau$ is the neutrino flavour index , i=1,2,3 is the mass eigenstate index and U is a unitary 3×3 matrix.

The inverse relation is

$$\nu_i = \sum_\alpha V_{i\alpha}\nu_\alpha \qquad (2)$$

where $V=U^{-1}=U^*$, that is $V_{i\alpha} = U^*_{\alpha i}$ since U is unitary.

Thus, the time evolution of a neutrino with momentum **p** , being at the state ν_α at time t=0 is given by

$$\nu(t) = e^{i\,\mathbf{p}\,\mathbf{r}} \sum_i U_{\alpha i}\, e^{-iE_i t}\nu_i \quad (3) \quad , E_i = \sqrt{p^2 + m_i^2}$$

If the 3 masses m_i are not all equal the state $\nu(t)$ has components ν_β with $\beta\neq\alpha$. So, a change of the neutrino flavour, that is a neutrino oscillation is possible.

We are interested essentially in the case of 2 neutrino mixing. Then U depends on a single real parameter θ :

$$U = \begin{bmatrix} \cos\theta & \sin\theta \\ -\sin\theta & \cos\theta \end{bmatrix}$$

Eqs. (1),(2) and (3) become respectively:

$\nu_\alpha = \cos\theta\,\nu_1 + \sin\theta\,\nu_2 \qquad (4a)$

$\nu_\beta = -\sin\theta\ \nu_1 + \cos\theta\ \nu_2$ (4b)

$\nu_1 = \cos\theta\ \nu_\alpha - \sin\theta\ \nu_\beta$ (5a)

$\nu_2 = \sin\theta\ \nu_\alpha + \cos\theta\ \nu_\beta$ (5b)

$\nu(t) = e^{ipr}\left(\cos\theta e^{-iE_1 t}\nu_1 + \sin\theta e^{-iE_2 t}\nu_2\right)$ (6) where $\nu(0) = \nu_\alpha$.

The probability to detect a neutrino state ν_β at time t is

$$P_{\alpha\beta}(t) = \left| \left\langle \nu_\beta \middle| \nu(t) \right\rangle \right|^2 = \sin^2 2\theta \sin^2\left(\frac{m_2^2 - m_1^2}{4p} t \right) \quad (7)$$

where we have used the approximation $E_i = \sqrt{p^2 + m_i^2} \approx p + \frac{m_i^2}{2p}$,valid for $m_i << p$.

The probability to detect a neutrino state ν_α if $\nu(0)=\nu_\alpha$ is $P_{\alpha\alpha}(t) = 1 - P_{\alpha\beta}(t)$ (8) .

Furthermore, if $\nu(0) = \nu_\beta$ we have in the same way $P_{\beta\alpha}(t) = P_{\alpha\beta}(t)$.

Eq. (7) can also be expressed in more familiar units as

$$P_{\alpha\beta}(L) = \sin^2 2\theta \sin^2\left(1.267 \frac{\Delta m^2}{E} L\right) \quad (9)$$

where

$L = ct$ [m] : the distance from the source

$\Delta m^2 = \left| m^2{}_2 - m_1^2 \right|$ [eV^2]

$E \approx p$ [MeV] : the neutrino energy

Eq. (9) also holds for L [km] and E [GeV] .

Eq. (9) describes an oscillation with amplitude $\sin^2 2\theta$ and oscillation length

$$\lambda = 2.48 \frac{E}{\Delta m^2} \quad (10)$$

where λ [m] if E [MeV] (λ [km] if E [GeV]) and Δm^2 [eV^2] .

If λ is much shorter than the size of the neutrino source or the detector or both then

$$\sin^2\left(1.267 \frac{\Delta m^2}{E} L\right) \approx \left\langle \sin^2\left(1.267 \frac{\Delta m^2}{E} L\right) \right\rangle = \frac{1}{2}$$

Then $P_{\alpha\beta}$ is independent of L : $P_{\alpha\beta} = \frac{1}{2}\sin^2 2\theta$ (11)

1.2 Neutrino oscillations in matter.

Wolfenstein first pointed out that neutrino oscillations in dense matter differ from oscillations in vacuum if ν_e 's are involved. The reason for this is the following : Coherent neutrino scattering at 0° has a Z-boson exchange amplitude which is the same for all 3 neutrino flavours. In the case of ν_e 's there is also a contribution from W-boson exchange with matter electrons.

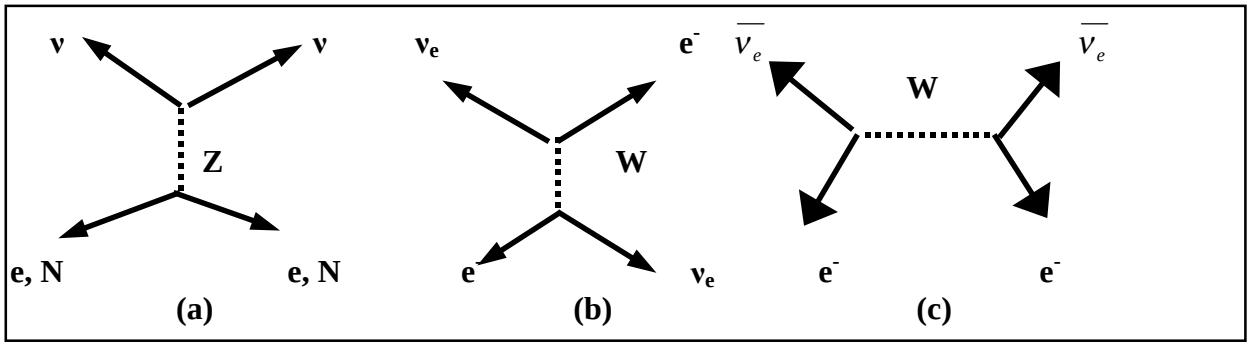

The propagation of neutrinos in matter can be described by adding to the Hamiltonian a potential energy term V_w.

For the process (c) : $V_w = \sqrt{2} G_F N_e \approx 7.63 \times 10^{-14} \frac{Z}{A} \rho$ eV (12)

where G_F is the Fermi coupling constant, N_e is the number of e^- per unit volume, ρ is the matter density in g/cm^3, Z is the atomic number and A the mass number of the material.

We are now going to consider the case of 2 neutrino mixing between ν_e and ν_μ :

$\nu_e = \nu_1 \cos\theta_v + \nu_2 \sin\theta_v$ (13a)

$\nu_\mu = -\nu_1 \sin\theta_v + \nu_2 \cos\theta_v$ (13b)

where θ_v is the mixing angle in vacuum. We assume that $\theta_v < 45°$ and $m_2 > m_1$.

The time dependent Schrodinger equation is

$$i\frac{d\Psi}{dt} = H\Psi \qquad (14)$$

$$\Psi = \begin{pmatrix} \nu_e \\ \nu_\mu \end{pmatrix} \qquad (15)$$

$$H = \sqrt{p^2 + M^2} + V_Z \begin{bmatrix} 1 & 0 \\ 0 & 1 \end{bmatrix} + V_W \begin{bmatrix} 1 & 0 \\ 0 & 0 \end{bmatrix} \qquad (16)$$

where M^2 is the square of the mass matrix and V_Z is the potential energy term resulting from Z-boson exchange.

Using the approximation $H = \sqrt{p^2 + M^2} \approx E + \frac{M^2}{2p}$ we have

$$H = (E + V_Z) \begin{bmatrix} 1 & 0 \\ 0 & 1 \end{bmatrix} + \frac{1}{2E} \begin{bmatrix} M^2_{ee} + 2EV_W & M^2_{e\mu} \\ M^2_{\mu e} & M^2_{\mu\mu} \end{bmatrix} \qquad (17)$$

where

$$M^2_{ee} = \frac{1}{2}(\mu^2 - \Delta m^2 \cos 2\theta_v) \qquad (18a)$$

$$M^2_{e\mu} = M^2_{\mu e} = \frac{1}{2}\Delta m^2 \sin 2\theta_v \qquad (18b)$$

$$M^2_{\mu\mu} = \frac{1}{2}(\mu^2 + \Delta m^2 \cos 2\theta_v) \qquad (18c)$$

$$\mu^2 = m^2_1 + m^2_2 \qquad (19)$$

$$\Delta m^2 = m^2_2 - m^2_1 \qquad (20)$$

It is obvious that the first term in the Hamiltonian does not produce any mixing between ν_e and ν_μ .

In a medium of constant density the Hamiltonian is time-independent and by diagonalizing the second matrix in Eq. (17) the mass eigenstates can be found. The 2 mass eigenvalues in matter are

$$m^2 = \frac{1}{2}(\mu^2 + \xi) \pm \frac{1}{2}\sqrt{(\Delta m^2 \cos 2\theta_v - \xi)^2 + (\Delta m^2)^2 \sin^2 2\theta_v} \qquad (21)$$

The mixing angle in matter θ_m is

$$\tan 2\theta_m = \frac{\Delta m^2 \sin 2\theta_v}{\Delta m^2 \cos 2\theta_v - \xi} \qquad (22)$$

where $\xi = 2V_W E \approx 1.526 \times 10^{-7}\, \rho E\, (Z/A)\ \ eV^2$ (23) , ρ [g/cm^3] and E [MeV] .

The oscillation length in matter is λ_m

$$\lambda_m = \lambda_v \frac{\Delta m^2}{\sqrt{\left(\Delta m^2 \cos 2\theta_v - \xi\right)^2 + \left(\Delta m^2\right)^2 \sin^2 2\theta_v}} \qquad (24)$$

where λ_v is the oscillation length in vacuum given by Eq. (10).

Resonant behaviour

For $\xi = \xi_{res} = \Delta m^2 \cos 2\theta_v$ (25) :

i) the denominator in Eq.(22) vanishes and $\theta_m = 45°$ (maximal mixing).

ii) the difference between the 2 mass eigenstates in Eq.(21) is $\Delta m^2 \sin 2\theta_v$ (minimal difference).

iii) the oscillation length in Eq. (24) is $\lambda_m = \lambda_v / \sin 2\theta_v$ (maximum value).

The figure below is given for small values of θ_v .For $\xi > \xi_{res}$ ν_2 is mostly ν_e while for $\xi < \xi_{res}$ ν_2 is mostly ν_μ .

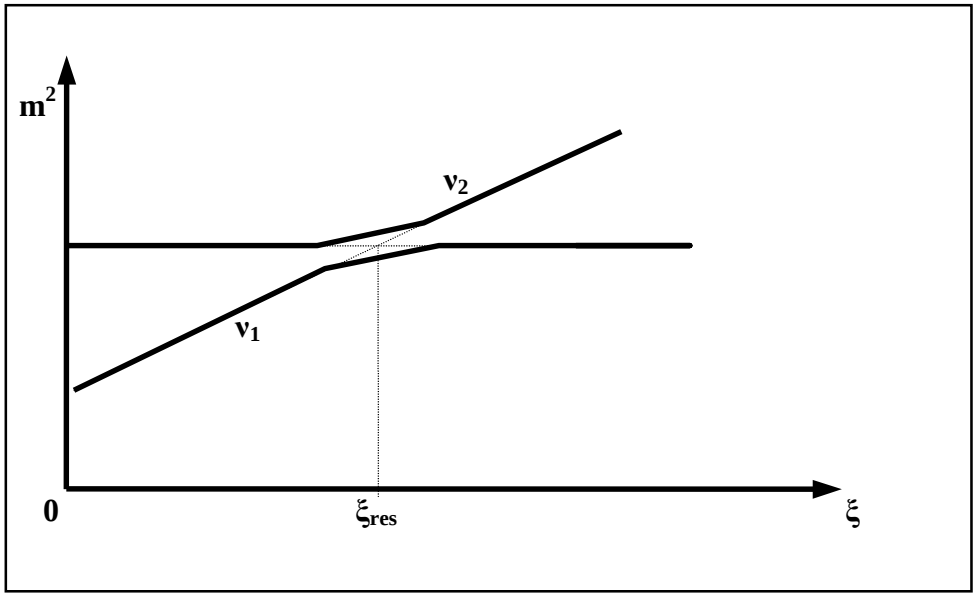

For $\overline{\nu_e}$ the potential energy term V_W changes sign (see the Feynman diagram (c)) and there is no resonance.

2.SOLAR NEUTRINOS AND RELATIVE EXPERIMENTS.

2.1 The Standard Solar Model (SSM)

There are several nuclear fusion reactions occurring in the Sun core all being summarized by $4p \rightarrow He^4 + 2e^+ + 2\nu_e$ (26).This reaction is followed by the annihilation of the 2 positrons with 2 electrons. The average energy produced by reaction (26) and emitted by the sun in the form of electromagnetic radiation is $Q = (4m_p - M_{He} + 2m_e)\, c^2 - \langle E(2\nu_e)\rangle \approx 26.1$ MeV where $\langle E(2\nu_e)\rangle \approx 0.59$ MeV is the average energy carried by the 2 neutrinos.

The rate of ν_e emission from the sun is $\frac{dN(\nu_e)}{dt} = \frac{2L_0}{Q} \approx 1.8 \times 10^{38}\ s^{-1}$ where

$L_0 = 3.846 \times 10^{26}$ W is the sun luminosity. The solar neutrino flux measured on Earth is then $\Phi_\nu = \frac{1}{4\pi d^2}\frac{dN(\nu_e)}{dt} \approx 6.4 \times 10^{10}\ cm^{-2}\ s^{-1}$, where d =1 AU = 1.496×10^{11} m.

The main assumptions of the Standard Solar Model are :

i) hydrostatic equilibrium ;

ii) energy production by fusion ;

iii) thermal equilibrium (i.e. the thermal energy production rate is equal to the luminosity);

iv) the energy transport inside the Sun is dominated by radiation.

Sun parameters

Luminosity	3.846×10^{26} W
Radius	6.96×10^5 Km
Mass	1.989×10^{30} Kg
Age	4.6×10^9 years
Core temperature T_c	$15.6 \times 10^6\ {}^0$K
Surface temperature T_s	$5773\ {}^0$K
Hydrogen content in the core (by mass)	34.1%
Helium content in the core (by mass)	63.9%

There are 2 main nuclear reaction cycles in the Sun core :

i)The pp cycle, responsible for 98.5% of the Sun luminosity. It involves the following reactions :

$p + p \rightarrow e^+ + \nu_e + d$ (a)

$p + d \rightarrow \gamma + He^3$ (b)

$He^3 + He^3 \rightarrow He^4 + p + p$ (c)

Reactions (a),(b),(c) represent 85% of the pp cycle. In the remaining 15% reaction (c) is replaced by the following sequence :

$He^3 + He^4 \rightarrow \gamma + Be^7$ (d)

$e^- + Be^7 \rightarrow \nu_e + Li^7$ (e)

$p + Li^7 \rightarrow He^4 + He^4$ (f)

In 1.9×10^{-3} of the cases reactions (e) and (f) are replaced by

$p + Be^7 \rightarrow \gamma + B^8$ (g)

$B^8 \rightarrow Be^8 + e^+ + \nu_e$ (h)

$Be^8 \rightarrow He^4 + He^4$ (i)

In 0.4% of the cases reaction (a) is replaced by the 3 body fusion reaction

$p + e^- + p \rightarrow d + \nu_e$ (j)

In ~$2.4\ 10^{-5}$ of the cases reaction (c) is replaced by

$He^3 + p \rightarrow He^4 + e^+ + \nu_e$ (k)

In the pp cycle ν_e 's are produced by 5 reactions and we denote the corresponding ν_e 's by different symbols :

Reaction	Neutrinos produced	Neutrino spectrum
(a)	ν_{pp}	Continuous
(e)	ν_{Be}	Mono-energetic
(h)	ν_B	Continuous
(j)	ν_{pep}	Mono-energetic
(k)	ν_{hep}	Continuous

ii)The CNO cycle. It involves the following reactions :

$p + N^{15} \rightarrow C^{12} + He^4$ (α)

$p + C^{12} \rightarrow \gamma + N^{13}$ (β)

$N^{13} \rightarrow e^+ + \nu_e + C^{13}$ (γ)

$p + C^{13} \rightarrow \gamma + N^{14}$ (δ)

$p + N^{14} \rightarrow \gamma + O^{15}$ (ε)

$O^{15} \rightarrow e^+ + \nu_e + N^{15}$ ($\sigma\tau$)

$p + N^{15} \rightarrow \gamma + O^{16}$ (ζ)

$p + O^{16} \rightarrow \gamma + F^{17}$ (η)

$F^{17} \rightarrow e^{+} + \nu_e + O^{17}$ (θ)

$p + O^{17} \rightarrow N^{14} + He^{4}$ (ι) followed by (ε) and $(\sigma\tau)$.

Production of ν_e 's occurs in reactions (γ),$(\sigma\tau)$ and (θ).These neutrinos are denoted as ν_N, ν_O and ν_F respectively.

The ν_{pp} flux is the dominant component but these neutrinos are difficult to detect because of their low energy.
In figure(1-1) the solar neutrino energy spectrum as calculated from the SSM is shown. The energy threshold for the capture reaction $\nu_e + (A,Z) \rightarrow e^{-} + (A,Z+1)$ for various isotopes is displayed as well.

2.2 The Homestake experiment.

Solar neutrinos were successfully detected for the first time in the Homestake experiment, by measuring the production rate of A^{37} from the capture reaction ν_e (solar) + $Cl^{37} \rightarrow e^{-} + A^{37}$ which occurs in a 390 m^2 tank of 615 tonnes of C_2Cl_4.The isotope Cl^{37} represents 24% of all natural chlorine, so there were 125 tonnes of Cl^{37} in the tank. The tank was deep underground to reduce A^{37} production by cosmic rays. The energy threshold for this reaction is 0.814 MeV, so this reaction is not sensible to the ν_{pp} component. The daily A^{37} production rate is of the order of 0.5 atoms/day. Every few months Argon is extracted from the tank, purified, mixed with natural Argon and used to fill a proportional counter. The presence of A^{37} in the counter is detected by observing its decay by electron capture

$e^{-} + A^{37} \rightarrow \nu_e + Cl^{37}$ (27) , $\tau_{1/2} = 34$ days.

It has become customary to express the solar neutrino capture rate in Solar Neutrino Units (SNU) : 1 SNU corresponds to 1capture /s from 10^{36} nuclei.
The weighted average of the Homestake experiment is
$R_{exp}(Cl^{37}) = 2.55 \pm 0.17 \pm 0.18$ SNU where the first error is statistical and the second one represents the systematic uncertainties.

The total rate for reaction (27) is predicted to be R_{th} (Cl^{37}) = 8.0 ± 3.0 SNU which disagrees with the measured value.

An independent SSM calculation predicts $R_{th}(Cl^{37})$ = 6.4 ± 1.4 SNU which is again larger than the measured value. The ratio of the measured value to the lower theoretical prediction is

$$\frac{R_{\exp}\left(Cl^{37}\right)}{R_{th}\left(Cl^{37}\right)} = 0.40 \pm 0.04 \pm 0.09 \quad (28)$$

where the first error is experimental and the second one represents the theoretical uncertainty. Eq.(28) illustrates the so-called solar neutrino problem.

2.3 The KAMIOKANDE experiment.

KAMIOKANDE is a real time experiment which uses an underground detector installed in the Kamioka mine near Tokyo.

The KAMIOKANDE detector is shown in figure(1-2). The inner detector consists of a cylindrical tank with a diameter of 15.6 m and a height of 11.2 m, filled with 2140 tonnes of water. Approximately 20% of the tank surface is covered by photomultipliers. The inner detector is surrounded by an additional layer of water seen by other photomultipliers and used to reject charged particles entering the detector from outside. The inner detector is used as an imaging Cerenkov counter. Charged particles with $\frac{v}{c} \approx 1$ produce Cerenkov light at an angle of ~ 41° to their direction of flight and the pattern of hit photomultipliers and their relative timing provide information on the particle direction and origin in the detector volume.

Solar neutrinos are detected by the scattering reaction $\nu_e + e^- \rightarrow \nu_e + e^-$ (29). The detection energy threshold is set by the requirement that at least 20 photomultipliers give a signal corresponding to at least one photo-electron. This requirement corresponds to a ν_e energy of 7.5 MeV and thus the experiment is sensitive mainly to the ν_B component. The detected electron from reaction (29) has a very strong directional correlation with the incident neutrino. This property is used to demonstrate the solar origin of the events.

KAMIOKANDE has taken data for a total of 1667 days. The neutrino flux, averaged over the entire period, is measured to be $\Phi_{\exp} = \left(2.9 \begin{matrix} +0.22 \\ -0.21 \end{matrix} \pm 0.35\right) \times 10^6 cm^{-2} s^{-1}$

where the first error is statistical and the second represents the systematic uncertainties.

This result is significantly lower than the SSM predictions

$\Phi_{th} = (5.7 \pm 0.7) \times 10^6 cm^{-2} s^{-1}$ or independently $\Phi_{th} = (4.9 \pm 1.0) \times 10^6 cm^{-2} s^{-1}$.

Thus KAMIOKANDE confirms the existence of the solar neutrino problem.

2.4 Gallium experiments.

Both the KAMIOKANDE and the Homestake experiments are sensitive to solar neutrinos of relatively high energy. These neutrinos represent only a small fraction of the total solar neutrino flux and questions have been raised on the reliability of the SSM predictions. On the contrary, the ν_{PP} component of the solar neutrino flux can be reliably predicted because these neutrinos originate from reactions (a) through (c) which are responsible for most of the Sun luminosity. A method to detect these neutrinos was proposed by Kuzmin who suggested to use the capture reaction

$\nu_e + Ga^{71} \rightarrow Ge^{71} + e^-$ (30) which has a neutrino energy threshold of 0.233MeV.

Two experiments (GALLEX and SAGE) have recently used this reaction to detect solar neutrinos.

The GALLEX experiment, installed deep underground in the Gran Sasso National Laboratory, uses 30.3 tonnes of natural Gallium, containing 39.6% of Ga^{71}, in the form of a water solution of gallium chloride. Every 3 weeks, $GeCl_4$ is extracted from the tank and chemically converted to GeH_4 gas. This gas is then introduced into a proportional counter built from special low-radioactivity materials and carefully shielded against natural relativity.

The presence of Ge^{71} from reaction (30) is then detected by observing its decay by electron capture $e^- + Ge^{71} \rightarrow Ga^{71} + \nu_e$ (31) , $\tau_{1/2}$ = 11.43 days.

The average value is $R_{exp}(Ga^{71}) = 79 \pm 10 \pm 6$ SNU where the first error is statistical and the second represents the systematic uncertainties.

The SAGE (Soviet-American Gallium Experiment) experiment, installed in Caucasus, uses metallic Gallium which is liquid at operating temperature, from which Ge^{71} is extracted and detected using reaction (31).

The most recent result is in good agreement with GALLEX :

$R_{exp}(Ga^{71}) = 69 \pm 11^{+5}_{-7}$ SNU where the first error is statistical and the second represents the systematic uncertainties.

The weighted average of the two experiments $R_{exp}(Ga^{71}) = 74 \pm 9.5$ SNU represents a deficit of ~40% with respect to the SSM predictions.

2.5 Interpretation of the solar neutrino problem.

Further research has indicated three possible explanations to the solar neutrino problem:

i) At least 2 of the 3 measurements of the solar neutrino flux are wrong.

ii) There is a basic flaw in the SSM, resulting in unreliable predictions of the solar neutrino flux.

iii) The ν_{Be} 's are produced as ν_e in the core of the Sun but are no longer ν_e when they reach the Earth.

This last explanation, which we assume to be the correct one, implies the occurrence of neutrino oscillations.

For neutrinos propagating through the Sun, the density ρ varies along the trajectory from a value higher than 100 g/cm^3 in the core to much less than 1 g/cm^3 in the outermost layers. The ratio Z/A also varies across the Sun because of the varying hydrogen abundance. Hence, in Eq.(14) the Hamiltonian depends on time. For a given set of mixing parameters m_1 , m_2 and θ_v Eq.(14) can be solved numerically with the initial condition $\Psi(0) = \begin{pmatrix} 1 \\ 0 \end{pmatrix}$ which represents a pure ν_e state, using the SSM predictions for the solar density, Z/A ratio and distribution of neutrino origins inside the Sun core.

The results from the latest analysis of the solar neutrino data in terms of matter enhanced oscillations are shown in figure(1-3). For each experiment the measured event rate corresponds to a region of allowed parameters in the ($\sin^2 2\theta_v$, Δm^2) plane. Since the processes used to detect solar neutrinos have different energy thresholds, these regions do not coincide and the oscillation parameters which describe all available data are defined by their overlap.

As shown in figure(1-3) the best fit values of the oscillation parameters taking into account matter effects are

$\sin^2 2\theta = 6.5\times10^{-3}$; $\Delta m^2 = 6.1\times10^{-6}$ eV^2

or $\sin^2 2\theta = 0.62$; $\Delta m^2 = 9.4\times10^{-6}$ eV^2

One must add to these two solutions the vacuum oscillation solutions for which Δm^2 is in the range $10^{-11} - 10^{-10}$ eV^2 and $\sin^2 2\theta > 0.7$ (see figure (1-4)).

2.6 Future experiments on solar neutrinos.

The SNO experiment.

The Sudbury Neutrino Observatory (SNO) is a solar neutrino detector under construction near Sudbury, Ontario.The detector consists of a spherical vessel containing ~1000 tonnes of high purity heavy water.Cerenkov light produced in the heavy water is collected by photomultipliers.

Solar neutrinos are detected by observing the reactions :

$\nu_e + d \rightarrow p + p + e^-$ (32)

$\nu_e + e^- \rightarrow \nu_e + e^-$ (33)

For both reactions the Cerenkov light ring produced by the electron is detected with a threshold of ~2MeV, which makes the experiment sensitive only to neutrinos from B^8 decay.

An additional feature of SNO is its anticipated capability to detect the reaction

$\nu + d \rightarrow p + n + \nu$ (34)

which has the same cross-section for all neutrino flavours and measures, therefore, the total solar neutrino flux. This reaction is observed by dissolving high purity $MgCl_2$ salt into the heavy water and by detecting the 8.5MeV γ-ray emitted by neutron capture in Cl^{35} :

$n + Cl^{35} \rightarrow Cl^{36} + \gamma$ (35)

In the absence of oscillations, one expects ~10^4 events/year from reaction (32), ~10^3 events/year from reaction (33) and ~3×10^3 events/year from reaction (34) with $MgCl_2$ salt. The presence of ν_e oscillations reduces the event rates from reactions (32) and (33) but does not change the rate of reaction (34).

BOREXINO experiment.

BOREXINO is a new experiment presently under construction at the Gran Sasso National Laboratory in Italy. The aim of the experiment is to detect the ν_e – electron

scattering reaction (33) with an energy threshold as low as 0.25 MeV. If this is achieved, the experiment is sensitive to the ν_{Be} component (E = 0.861 MeV) which is expected to be strongly suppressed if neutrino oscillations are the solution of the solar neutrino problem. In the absence of oscillations one expects ~50 events/day from these neutrinos.

3.ATMOSPHERIC NEUTRINOS AND RELATIVE EXPERIMENTS.

Since the total thickness of the atmosphere is ~ 10^3 g/cm^2 ,which is equivalent to ~ 10 interaction lengths, the interaction of a primary cosmic ray in the upper layers of the atmosphere results in the development of a hadronic shower leading to a flux of neutrinos from charged pion and muon decay. These neutrinos have energies ranging from ~ 0.1 GeV to a few GeV.

Since a ν_μ is produced from both $\pi^\pm$ and μ^+ decay , and a ν_e from $\mu^\pm$ decay only, one expects the ratio between the ν_μ and ν_e fluxes on Earth to be of the order of 2. However, the calculations of the atmospheric neutrino fluxes are affected by sizeable uncertainties which result from uncertainties on the composition and energy spectrum of the primary cosmic rays, on secondary particle distributions and on the K/π ratio. The final uncertainty affecting the ν_μ and ν_e fluxes on Earth is of the order of ± 30%. However, the uncertainty on the predicted ν_μ/ν_e ratio is believed to be less than ± 10%.

Five underground experiments have measured the atmospheric neutrinos fluxes by detecting quasi-elastic interactions :

$$\nu_\mu(\nu_e) + n \rightarrow \mu^-(e^-) + p \qquad (36)$$

$$\overline{\nu_\mu}(\overline{\nu_e}) + p \rightarrow \mu^+(e^+) + n \qquad (37)$$

Two of these experiments (KAMIOKANDE and IMB-3) are based on large volume water tanks and detect the Cerenkov light ring produced by relativistic particles in water. The other 3 experiments (FREJUS, NUSEX and SOUDAN-2) use calorimeters with long longitudinal and transverse segmentation .

The comparison between the measured and predicted ν_μ/ν_e ratio for the 5 experiments gives an average

$$\frac{(\nu_\mu/\nu_e)_{measured}}{(\nu_\mu/\nu_e)_{predicted}} = 0.61 \pm 0.06 \quad (38)$$

The deviation of this ratio from 1 illustrates the so-called atmospheric neutrino problem.

The comparison between the measured and predicted results shows that the ν_μ flux is lower than predicted while the ν_e flux agrees with the calculations. This could just be the effect of the large uncertainties affecting these calculations. However, an interpretation of these results in terms of neutrino oscillations is also possible. In this case, ν_μ -ν_τ and ν_μ-ν_e oscillations are both acceptable solutions.

Additional evidence in favour of neutrino oscillations has been reported by KAMIOKANDE. Since the flux of atmospheric neutrinos on Earth is,to a good approximation, isotropic, the neutrino flight path from the production point to the detector varies enormously with the zenith angle θ. For example, neutrinos impinging on the detector from above ($\cos\theta = 1$) are produced few km above the detector, while upward going neutrinos ($\cos\theta = -1$) have travelled for at least the Earth diameter (13,000 km) before reaching the detector. Hence, oscillations may result in a dependence of the ν_μ/ν_e ratio on the zenith angle θ. This dependence was confirmed by KAMIOKANDE for multi-GeV neutrinos and the results were consistent with the theoretical expectations for :

ν_μ - ν_e oscillations with $\Delta m^2 = 0.018\ eV^2$ or

ν_μ - ν_τ oscillations with $\Delta m^2 = 0.016\ eV^2$ and $\sin^2 2\theta \geq 0.6$.

SURER-KAMIOKANDE is a new, very massive water Cerenkov detector .It studies solar and atmospheric neutrinos and is taking data since 1996 .The solar neutrino event rate is ~30/day and the atmospheric neutrino event rate is ~2000 /year.

4. NEUTRINO OSCILLATION EXPERIMENTS.

4.1 Neutrino oscillation experiments in general.

There are 2 types of experiments searching for neutrino oscillations :

Disappearance experiments.

The probability measured by these experiments is

$$P_{\alpha\alpha}(L) = 1 - \sum_{\beta \neq \alpha} P_{\alpha\beta}(L) \quad (39)$$

The flux of a given neutrino flavour is measured at a distance L from the source. The presence of neutrino oscillations has the effect of reducing this flux with respect to the value expected in the absence of neutrino oscillations. The sensitivity of these experiments is limited by the systematic uncertainty on the knowledge of the neutrino flux from the source. In order to measure directly the neutrino flux from the source a second detector close to the source is often used .

These experiments have been performed at nuclear reactors and at accelerators. The core of a nuclear reactor is an intense source of $\overline{\nu}_e$ with an average energy of ~3MeV,which can be detected by observing the reaction $\overline{\nu}_e + p \rightarrow e^+ + n$.

If a $\overline{\nu}_e$ turns into a $\overline{\nu}_\mu$ or a $\overline{\nu}_\tau$ it becomes invisible because μ^+ or τ^+ production is energetically forbidden. Proton accelerators produce ν_μ 's with energies between ~30MeV and ~200GeV.The ν_μ flux is measured by detecting the reaction $\nu_\mu + \text{nucleon} \rightarrow \mu^- + \text{hadrons}$. It can be noted that the energy threshold for $\nu_\mu + n \rightarrow \mu^- + p$ on a neutron at rest is 110.2 MeV.

Appearance experiments.

These experiments use beams containing predominantly one neutrino flavour and search for neutrinos of different flavour at a certain distance from the source. The sensitivity of these experiments is limited by the systematic uncertainty on the knowledge of the beam contamination by other neutrino flavours at the source. For example, in a typical ν_μ beam from a high energy accelerator the ν_e contamination at the source is of the order of 1%.

These experiments are performed at accelerators and they search for ν_e 's and ν_τ 's in a beam containing predominantly ν_μ 's.The presence of ν_e 's (ν_τ 's) in the beam is detected by observing the reaction ν_e (ν_τ) + nucleon $\rightarrow e^-$ (τ^-) + hadrons.

So far, searches for neutrino oscillations at nuclear reactors or at proton accelerators have failed to observe any oscillation signal. These negative results set upper limits for the oscillation probability which can be converted into excluded regions in the oscillation parameter plane ($\sin^2 2\theta, \Delta m^2$) using Eq.(1-9) [or Eq.(1-11) if Δm^2 is large]. In figures (1-5),(1-6) and (1-7) the excluded region is on the right of the corresponding curve.

4.2 Oscillation experiments at nuclear reactors.

Two $\overline{\nu_e}$ disappearance experiments are presently under construction at the Chooz (France) and San Onofre (California) nuclear power plants.

The Chooz detector, installed in an underground tunnel, consists of 3 concentric vessels. The innermost one contains 4.9 tonnes of Gadolinium doped liquid scintillator which acts as the $\overline{\nu_e}$ target and as a detector. The 2 other vessels are both filled with liquid scintillator.

The San Onofre detector, consists of 12 tonnes of Gadolinium loaded scintillator surrounded by 1m thick water shield and by a liquid scintillator layer to reject cosmic rays. The central detector is subdivided into cells.

In both experiments the reaction $\overline{\nu_e} + p \rightarrow e^+ + n$ produces a prompt e^+ signal followed by a delayed photon signal resulting from neutron capture in Gadolinium. Both experiments are sensitive to $\overline{\nu_e}$ oscillations with Δm^2 values in the range from 3×10^{-3} eV^2 to 3×10^{-2} eV^2 and $\sin^2 2\theta > 0.1$. In the Chooz detector the middle vessel is used to increase the photon detection efficiency. In the San Onofre detector the e^+ and the 2 photons from e^+ annihilation are detected in 3 neighbouring cells.

4.3 Oscillation experiments at accelerators.

4.3.1 Searches for $\nu_\mu - \nu_e$ oscillations.

The LSND experiment.

The Liquid Scintillator Neutrino Detector has reported the observation of events which can be interpreted in terms of $\nu_\mu - \nu_e$ oscillations.

Protons from the LAMPF (Los Alamos Meson Physics Facility) 800 MeV linear accelerator produce pions in a 30 cm long water target located ~1 m upstream of a copper beam stop.

Neutrinos are produced by the following processes :

$\pi^+ \rightarrow \mu^+ + \nu_\mu$ (in flight or at rest) (40a)

$\mu^+ \rightarrow e^+ + \overline{\nu_\mu} + \nu_e$ (at rest) (40b)

$\pi^- \rightarrow \mu^- + \overline{\nu_\mu}$ (in flight) (40c)

$\mu^- \rightarrow e^- + \nu_\mu + \overline{\nu_e}$ (at rest) (40d)

The relative yield of $\overline{\nu_e}$ above an energy of 36 MeV is only ~ 4×10^{-4} because π^- decaying in flight are only a few % of all produced π^- and only a small fraction of the μ^- stopping in high Z material undergoes decays (π^- at rest do not decay because they are immediately captured by nuclei).

LSND detects $\overline{\nu_e}$ by the reaction $\overline{\nu_e} + p \rightarrow e^+ + n$ (41) which gives a prompt e^+ signal followed by a delayed 2.2 MeV γ-ray from the capture reaction

$n + p \rightarrow d + \gamma$ (42).

A total of 9 events has been observed in the e^+ energy interval 36 – 60 MeV , to be compared with an expected background of 2.12 ± 0.34 events for 2 run-times. However, an independent analysis of the same data reports the observation of 5 events to be compared with an expected background of 6.2 events. In view of the limited statistical evidence of the LSND experiment and of the existence of 2 independent analyses reaching different conclusions, it is not possible at present to consider the LSND result as evidence from $\nu_\mu - \nu_e$ oscillations. More data are needed to reach a definite conclusion.

The KARMEN experiment.

The Karlsruhe-Rutherford Medium Energy Neutrino experiment is similar to the LSND experiment and is performed at the spallation neutron facility ISIS of the Rutherford-Appleton Laboratory. An important difference of ISIS with respect to LAMPF is that the ISIS beam (800 MeV protons) is pulsed with a time structure consisting of two 100 ns long pulses separated by 320 ns, with a repetition rate of 50 Hz. Thus it is possible to separate neutrinos from muon and pion decay using their different time distributions with respect to the beam pulse.

The KARMEN experiment has observed no signal above the expected background from reaction (41), providing no evidence for $\nu_\mu - \nu_e$ oscillations.

Figure (1-8) shows the allowed regions of the oscillation parameter plane for different experiments.

4.3.2 Searches for $\nu_\mu - \nu_\tau$ oscillations.

(A) The 'see-saw' model.

The so called 'see-saw' model is a reasonable theoretical proposal which tries to explain why neutrinos are much lighter than the charged leptons or quarks in the same fermion generation.

Going into the details of the 'see-saw' model is not our purpose; we just note the following conclusion : The eigenvalues of the square of the mass matrix in Eq.(17) give the mass values of the 2 physical neutrino states for each generation and it is

$m_1 \cong \frac{m^2}{M}$ and $m_2 \cong M$ where m and M are parameters of the theory with m << M.

A useful conclusion of the 'see-saw' model is that the $\nu_\mu - \nu_\tau$ oscillation length for a neutrino beam energy of 30 GeV would be in the range from 100m to 20km. Such oscillations can be observed using high-energy neutrino beams from accelerators if the mixing angle is not too small.

(B) The CERN experimental programme on ν_μ-ν_τ oscillations.

Two experiments (CHORUS and NOMAD), located at the CERN West Area Neutrino Facility (WANF), are presently taking data with the aim of detecting ν_μ -ν_τ oscillations.

The method adopted by both experiments consists in detecting τ^- production with a sensitivity corresponding to a ν_τ / ν_μ ratio of ~ 2×10^{-4} .Such a value is approximately 3 orders of magnitude larger than the value expected from D_S production by the primary proton beam, followed by the decay $D_S \rightarrow \tau^- + \nu_\tau$ .The observation of τ^- production could only result, therefore, from ν_μ -ν_τ oscillations.

Layout of the WANF beam line.

The layout of the WANF beam line is shown in Figure (1-9).

- A beam of 450 GeV protons is extracted from the SPS (Super Proton Synchrotron) and impinges on a beryllium target. Secondary particles are produced from the hadronic interactions in the beryllium target.

The SPS cycle repeats every 14.4 s. The protons are extracted from the SPS in two 4 ms long spills (fast/slow extraction) separated by 2.6 s with a 2.0 s “flat top” .The proton beam has a Gaussian shape with $\sigma \approx 0.5$ mm at the target. The beam line has been operating for 3 years now with record intensities up to 1.5×10^{13} protons in each of the two spills. The Beam Current Transformer (BCT) upstream of the target measures the flux of incident protons, while the downstream Secondary Emission Chamber (SEM) measures the total flux of secondary particles in the forward direction. The ratio of pions to kaons produced from protons interacting in the target is roughly 10:1.

- A pair of pulsed magnetic lenses (horn and reflector) located after the target produces a parallel wide-band beam of positive hadrons. The neutrinos are primarily produced from the decays in flight of the secondary π^+ and K^+ (hence the name neutrino parent particles).

A small-angle collimator was installed immediately after the target in order to better match the secondary particle beam to the entrance apertures of the magnetic elements (horn and reflector) downstream. The sections between the horn and reflector have been enclosed in He tubes in order to reduce the absorption of the secondary particles. A large-angle collimator has been installed between the horn and reflector to reduce the antineutrino contamination by intercepting the defocused negative secondaries before they decay. The mesons are allowed to decay in a 290 m long vacuum tunnel.

The mean free path for pions is about 55 m/GeV and for kaons around 7.5 m/GeV. The average neutrino energy produced in a pion decay is some 43% of the pion energy whereas for kaons the neutrino has, on average, some 95% of the parent kaon energy. Thus for a decay path of some 600m only 40% of the 23 GeV pions will have decayed to give neutrinos of about 10GeV whereas essentially all kaons of 10GeV will have decayed. Shielding made from iron and earth follows to range out the muons and absorb the remaining hadrons.

- A toroidal magnet, operated at 3 kA , located at the entrance of the iron shielding bends muons which would pass outside the shielding either further outwards or back into the iron plug which provides sufficient absorption. A neutrino beam monitoring system (the muon pits), based on the detection of muon yields at several depths in the iron shield, is built into the line.

- CHORUS and NOMAD detectors are installed one behind the other at a distance of ~ 820 m from the proton target.

The expected neutrino flux from the CERN wide-band beam for a fiducial area of 2.6×2.6 m^2 and for 10^9 protons on target (p.o.t) is shown in figure (1-10). The neutrino beam simulation is affected by uncertainties due mostly to the limited knowledge of the π and K yields from the hadronic interactions in the beryllium target. The measurement by the SPY (Secondary Particle Yields) collaboration of the production rates of π and K mesons and of their ratio has reduced these uncertainties.

The CHORUS experiment.

The CHORUS (CERN Hybrid Oscillation Research apparatUS) experiment aims at detecting the characteristic decay of the short-lived τ lepton in nuclear emulsion.

The detector is shown in figure (1-11).It consists of an emulsion target with a total mass of ~ 800 kg followed by an electronic tracking detector made of scintillating fibres, an air-core hexagonal magnet, high-resolution calorimeter and a muon spectrometer.

The hexagonal magnet provides a field of 0.1 T, over a length of 0.75 m, oriented along the sides of an hexagon with no radial dependence. It is used to determine the charge and momentum of low-energy particles with a resolution $\sigma(p) / p \sim 20\%$ for momenta between 2 and 10 GeV.

The calorimeters provide a resolution $\frac{\sigma(E)}{E} \sim \frac{013}{\sqrt{E}}$ and $\sim \frac{035}{\sqrt{E}}$ (E in GeV) for electromagnetic and hadronic showers, respectively.

Neutrino events with a μ^-, a negatively charged hadron or 3 charged hadrons with negative total charge are selected and one of the tracks is followed back to the exit point from the emulsion target for further scanning and measurement. The large number of ν_μ charged-current (CC) or neutral-current (NC) interactions which would satisfy this first selection is reduced by more than one order of magnitude by applying kinematical criteria which distinguish these events from ν_τ CC interactions. For a total 2.4×10^{19} protons on target, which correspond to a run of 2 years, one expects 5×10^5 ν_μ CC interactions in the emulsion target, which are reduced to $\sim3\times10^4$ events to be scanned by rejecting event configurations with the muon momentum and the total momentum of all other detected particles at opposite azimuthal angles. Similarly, the expected number of 1.5×10^5 ν_μ NC interactions is reduced to $\sim10^4$ events to be scanned by rejecting the events in which the missing transverse momentum is opposite in azimuth to the momentum of the negative hadron (or of the 3 charged hadrons).

Excellent space resolution can be achieved by means of the emulsion technique. Using a computer-assisted microscope, it is possible to analyze $\sim5 \times10^4$ events/year. Figure (1-12) shows the expected configuration of a typical ν_τ $N \rightarrow \tau^- X$ event in the emulsion and scintillating fibre tracker. The average τ^- decay length is ~1mm.

CHORUS sensitivity to ν_τ CC interactions. The number of events corresponds to a run of 2.4×10^{19} protons on target. N_τ is the number of events expected from ν_μ -ν_τ oscillations with $\Delta m^2 > 40$ eV^2 and $\sin^2 2\theta = 5\times10^{-3}$.

τ^- decay mode	Branching ratio	Efficiency	N_τ	Background events
$\nu_\tau\ \mu^-\ \overline{\nu_\mu}\ \overline{\nu_\mu}\ \overline{\nu_\mu}$	0.0178	0.084	20	0.15
$\nu_\tau\ h^- + n\ \pi^0$	0.50	0.040	25	0.5
$\nu_\tau \pi^-\ \pi^-\ \pi^+ + n\ \pi^0$	0.14	0.055	10	0.5
Total			55	1.15

The NOMAD experiment.

The NOMAD (Neutrino Oscillation Magnetic Detector) experiment aims at identifying τ^- production and decay using only kinematical criteria.

NOMAD detector is shown in figures (1-13) and (1-14). It is based on the UA1 magnet which provides a horizontal magnetic field of 0.4T perpendicular to the beam axis over a volume of $3.6\times3.5\times7.0$ m^3 .

The main detector components are :

i) A system of drift chambers, each with a thickness equivalent to ~0.02 radiation lengths and consisting of 3 wire planes for stereo reconstruction of charged particle tracks. These chambers also act as the neutrino target. The average density of this target is 0.1 g/cm^3.The momentum resolution for charged hadrons and muons is $\frac{\sigma(p)}{p} \approx \frac{0.05}{\sqrt{L}} \oplus \frac{0.008\,p}{\sqrt{L^5}}$ where L is the track length in m and p is the particle momentum in GeV. In this expression the first term arises from multiple scattering and the second one from measurement errors.

ii)Nine modules of transition radiation detectors (TRD) for electron identification. Each module detects the transition radiation X-rays produced by charged particles with E /m > 10^3 when they cross the radiator. Additional drift chambers are interspersed among the TRD modules to track charged particles in this region.

iii)An electromagnetic calorimeter with energy resolution $\frac{\sigma(E)}{E} \approx \frac{0.03}{\sqrt{E}} \oplus 0.01$

(E in GeV) for electrons and photons.

iv)A hadronic calorimeter.

v)Ten large-area muon chambers separated by a thick iron wall.

The NOMAD experiment aims at detecting τ^- production by observing both leptonic and hadronic decay modes of the τ^-.

The decay $\tau^- \rightarrow \nu_\tau + e^-$ is particularly attractive because the main background results from ν_e CC events which are only ~1% of the total number of neutrino interactions in the target fiducial volume. This background is rejected by kinematical considerations.

The decay $\tau^- \rightarrow \nu_\tau + \mu^- + \overline{\nu_\mu}$ has a much larger background but it can be reduced to a tolerable level at the expense of detector efficiency. The search for the hadronic decay modes $\tau^- \rightarrow \nu_\tau + \pi^-$, $\tau^- \rightarrow \nu_\tau + \rho^-$, $\tau^- \rightarrow \nu_\tau + \pi^- + \pi^- + \pi^+$ is also possible.

NOMAD sensitivity to ν_τ CC interactions. The number of events corresponds to a run of 2.4×10^{19} protons on target. N_τ is the number of events expected from ν_μ - ν_τ oscillations with $\Delta m^2 > 40 eV^2$ and $\sin^2 2\theta = 5 \times 10^{-3}$.

τ^- decay mode	Branching ratio	Efficiency	N_τ	Background events
$\nu_\tau e^-$	0.0178	0.135	39	4.6
$\nu_\tau \mu^-$	0.0178	0.039	11	2.2
$\nu_\tau \pi^-$	0.11	0.014	3	< 0.2
$\nu_\tau \rho^-$	0.23	0.020	7	< 0.2
$\nu_\tau \pi^- \pi^- \pi^+ + n \pi^0$	0.138	0.077	18	< 0.2
Total			78	6.8

Figure (1-15) shows the region of the ($\sin^2 2\theta, \Delta m^2$) plane excluded by the combined CHORUS and NOMAD results if no signal is seen in either experiment. The exclusion regions from previous experiments are also shown.

For $\Delta m^2 > 40 eV^2$ the limit on the ν_μ-ν_τ mixing angle is $\sin^2 2\theta < 2.3 \times 10^{-4}$ which represents an improvement by more than a factor of 20 with respect to the existing limits.

(C) Future experiments searching for ν_μ -ν_τ oscillations.

Short base-line experiments.

- COSMOS (Femilab).

A new experiment, named COSMOS has been recently approved at Fermilab. It will use the neutrino beam which will become available at Fermilab when the new Main Injector (MI) will start operation. COSMOS will start data taking around the year 2000. It expects to collect 6.3×10^6 ν_μ CC events in a run of 4 years. The corresponding number of events to be scanned is $\sim 1.5 \times 10^5$.

The COSMOS experiment is conceptually similar to CHORUS. The two main differences with respect to CHORUS are a more intense neutrino beam and the magnetic spectrometer which provides a better momentum resolution (σ_p / p ~3% to be compared with ~20% for the CHORUS hexagonal magnet).

	CERN SPS	**FERMILAB MI**
Proton energy	450 GeV	120 GeV
Protons on target/cycle	2×10^{13}	6×10^{13}
Cycle time	14.4 s	1.9 s
Protons on target/year	1.2×10^{19}	3×10^{20}
Average energy of interacting ν_μ	40 GeV	16 GeV

Figure (1-16) shows the region of the ($\sin^2 2\theta, \Delta m^2$) plane which will be excluded by COSMOS if no oscillation signal is observed. It will improve the anticipated CHORUS and NOMAD limit by an order of magnitude.

Long base-line experiments.

- MINOS (Fermilab -Soudan).

The neutrino beam from the Fermilab Main Injector is directed towards the Soudan underground laboratory in Minnesota at a distance of 730 km from Fermilab. The MINOS (Main Injector Neutrino Oscillation Search) detector will be installed in the Soudan laboratory and a second detector of similar conceptual design but much lighter will be installed at a distance of ~1 km from the proton target. MINOS will start data taking in parallel with the short base-line COSMOS experiment.

MINOS uses several methods to detect ν_μ -ν_τ oscillations. One method consists of measuring the ratio of the number of events with no muon to the number of events with one muon. If ν_μ -ν_τ oscillations are present this ratio will be different for the far and near detector because only ~18% of the ν_τ CC events will produce a μ^- from $\tau^- \rightarrow \nu_\tau + \mu^- + \overline{\nu_\mu}$ decay. An alternative, independent method consists in measuring the neutrino energy spectrum in both the far and near detector by measuring the total visible energy in events containing a μ^-.The presence of ν_μ - ν_τ oscillations would then result in a distortion of the spectrum measured in the far detector with respect to the spectrum measured in the near detector ; this distortion also provides a determination of oscillation parameters.
MINOS will be able to demonstrate the presence of ν_μ -ν_τ oscillations for mixing angles $\sin^2 2\theta > 0.01$ and $\Delta m^2 > 10^{-3}$ eV^2 .

- ICARUS (CERN-Gran Sasso).

An other long base-line experiment, being actually planned in Europe, consists in aiming a neutrino beam from the CERN SPS to the Gran Sasso National Laboratory in Italy at a distance of 732 km from CERN. ICARUS detector is installed in the Gran Sasso laboratory.
The layout of the CERN to Gran Sasso beam line is given in figure (1-17).
Figure (1-18) is the vertical cut showing the main components of the beam line.

ICARUS is a new detector concept based on a liquid Argon Time Projection Chamber (TPC) which allows 3-dimensional reconstruction of events with spatial resolution of the order of 1mm. Primary ionisation electrons drift in very high purity Argon over distances of the order of 1m and are collected by electrodes which provide two of the three coordinates and measure the ionisation, while the third component along the drift direction is determined by measuring the drift time.

After one year of data taking ICARUS should be able to exclude ν_μ -ν_τ oscillations with $\Delta m^2 > 2 \times 10^{-2}$ eV^2 and $\sin^2 2\theta > 0.1$ if no signal is observed. The oscillation parameter range to be covered is shown in figure (1-19).

Figure (1-1)

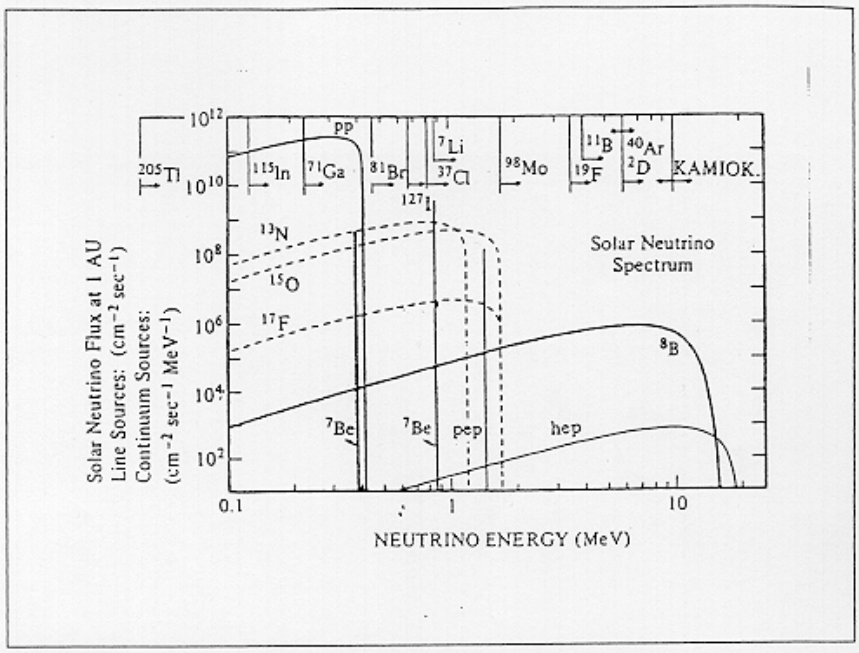

The solar neutrino energy spectrum as calculated from the SSM . The energy threshold for the capture reaction $\nu_e + (A,Z) \rightarrow e^- + (A,Z+1)$ for various isotopes is displayed as well.

Figure (1-2)

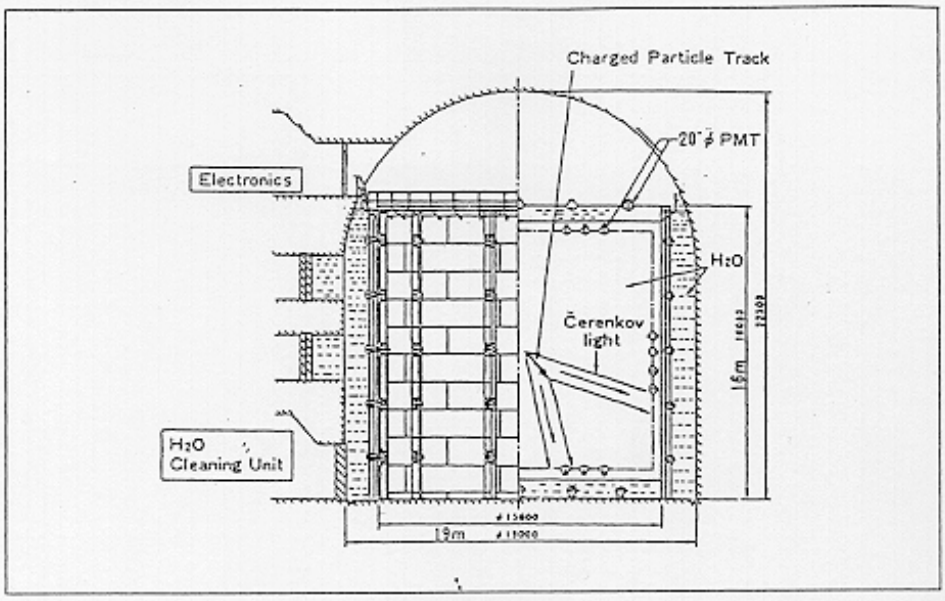

The KAMIOKANDE detector.

Figure (1-3)

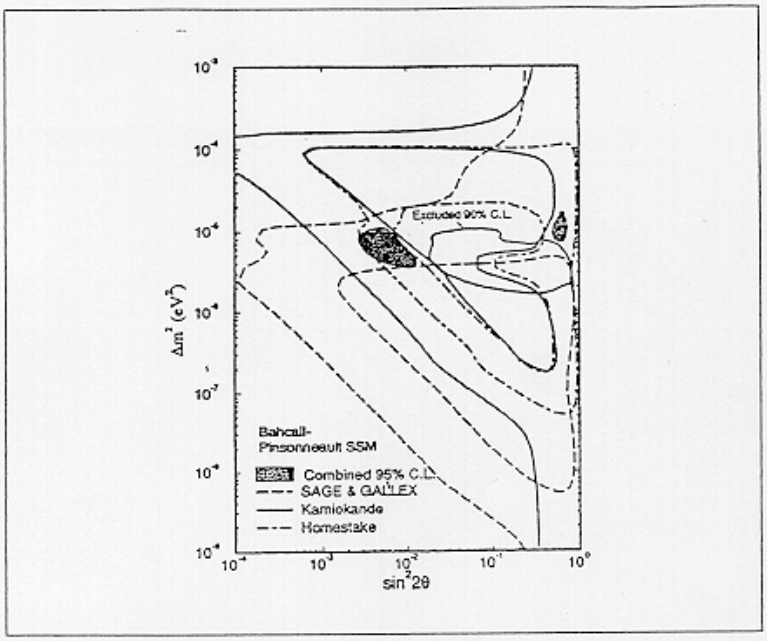

The allowed regions of different solar neutrino experiments using the SSM predictions.

Figure (1-4)

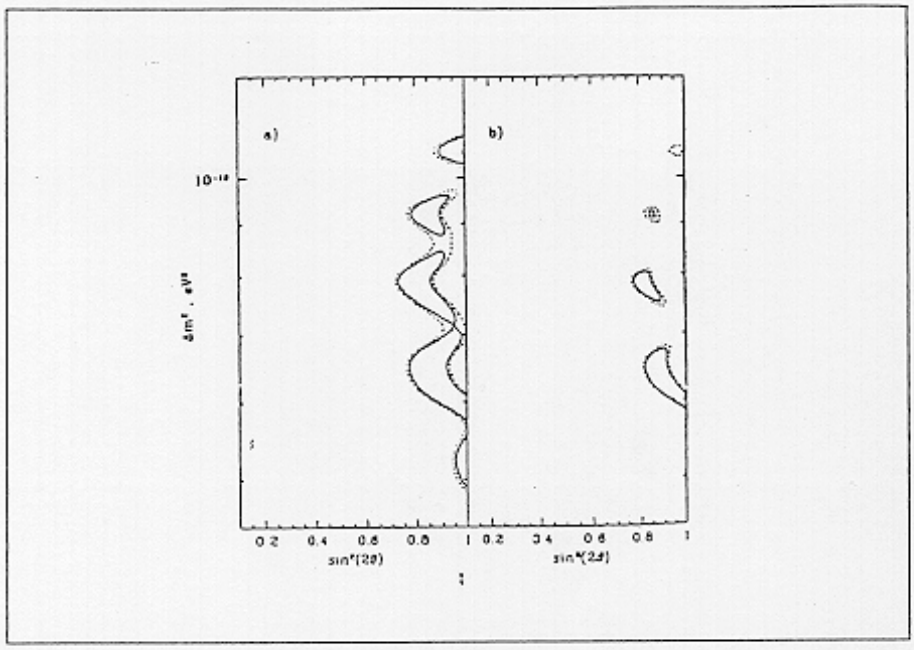

Regions of the ($\sin^2 2\theta, \Delta m^2$) plane allowed at the 90% (solid line) and 95% (dashed line) confidence level by the solar neutrino results using the SSM predictions including (a) or without including (b) the theoretical uncertainties.

Figure (1-5)

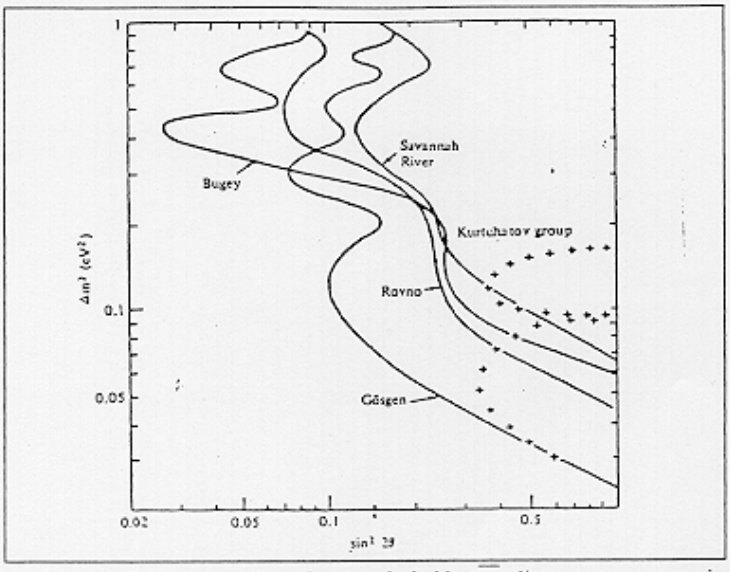

Regions of the oscillation parameter plane excluded by $\overline{\nu_e}$ disappearance experiments at nuclear reactors.

Figure (1-6)

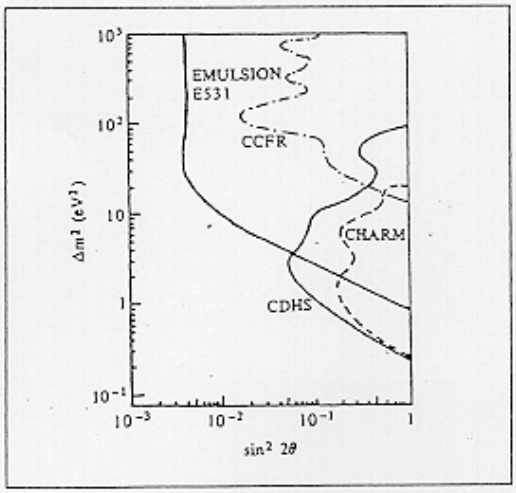

Exclusion regions in the oscillation parameter plane from ν_μ disappearance experiments (CCFR,CDHS,CHARM) and from a search for ν_τ appearance experiments using a ν_μ beam (EMULSION E531).

Figure (1-8)

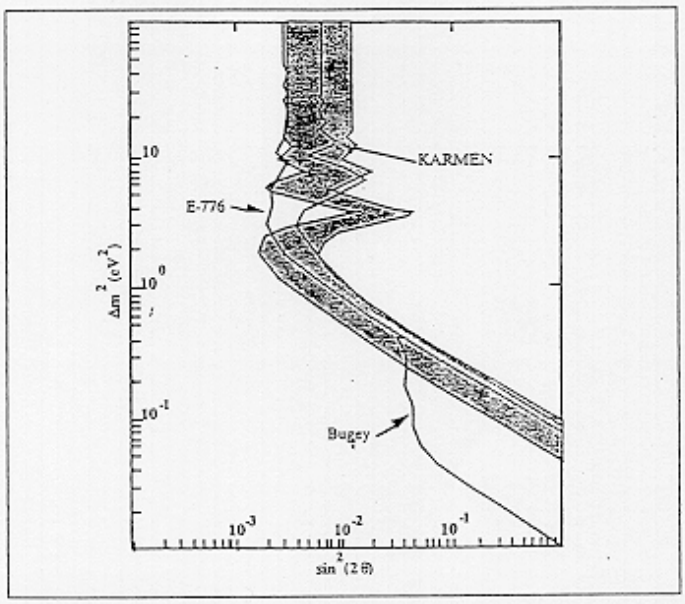

The allowed regions of the oscillation parameter plane for different $\nu_\mu - \nu_e$ oscillation experiments.

Figure (1-9)

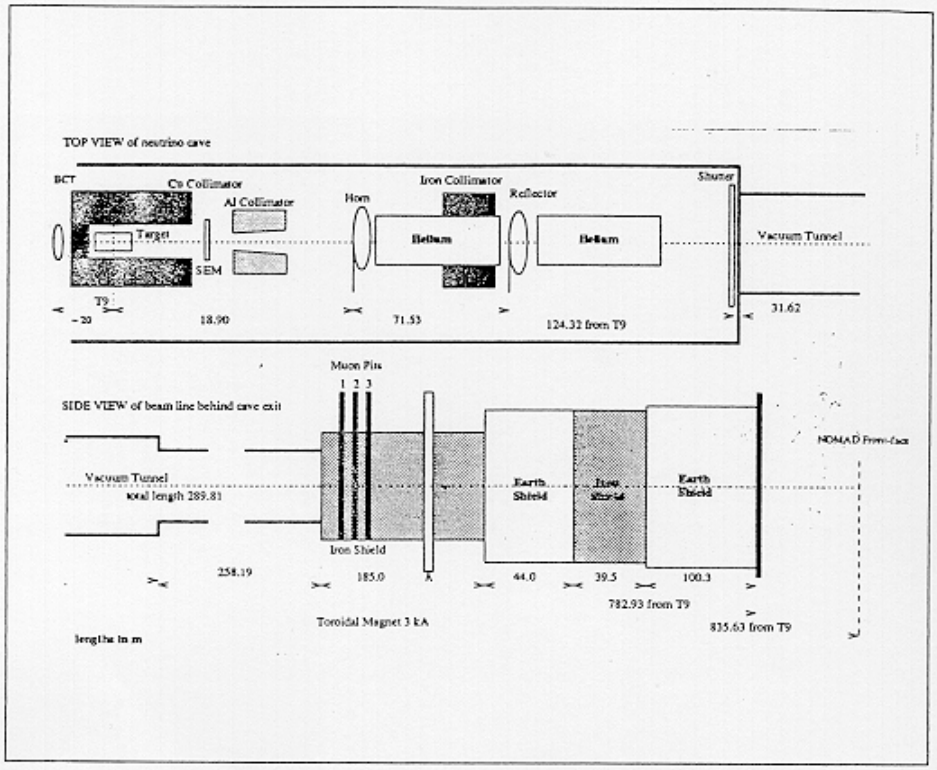

The layout of the WANF beam line.

Figure (1-10)

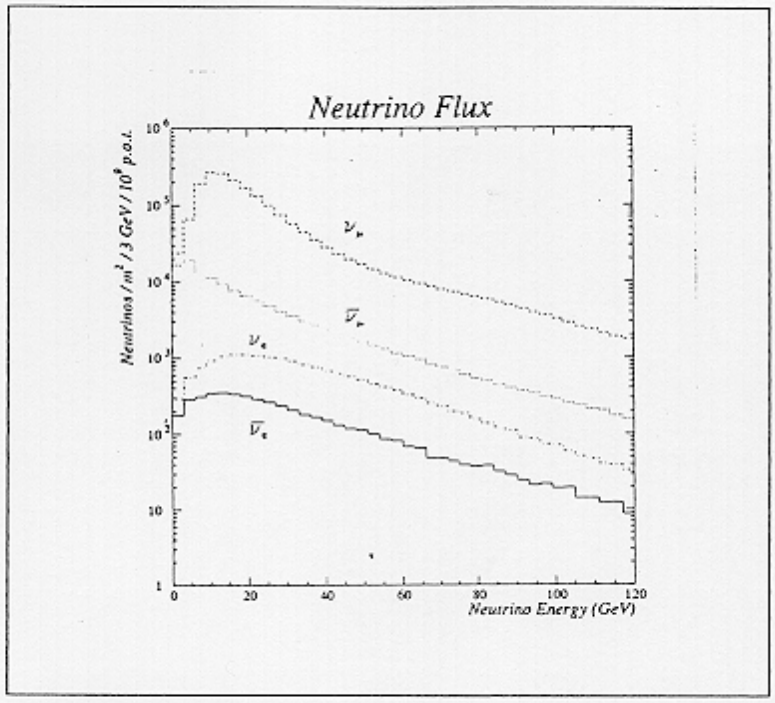

The expected neutrino flux from the CERN wide-band beam for a fiducial area of 2.6×2.6 m^2 and for 10^9 protons on target (p.o.t).

Figure (1-11)

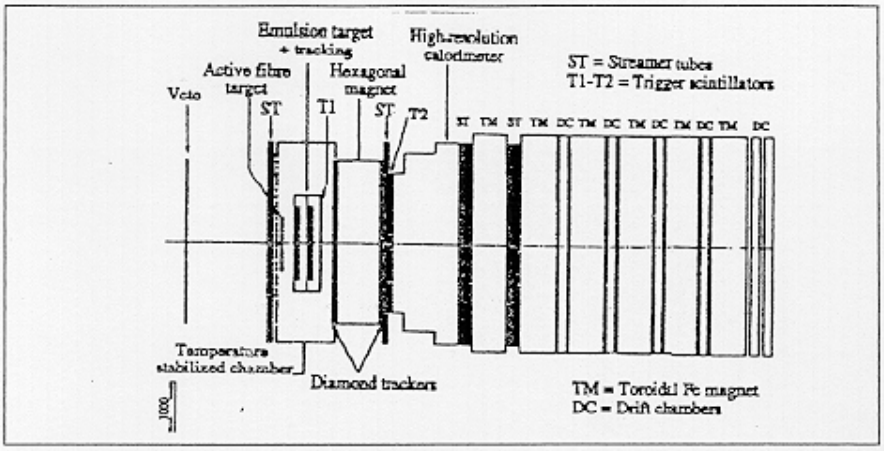

The CHORUS detector

Figure (1-12)

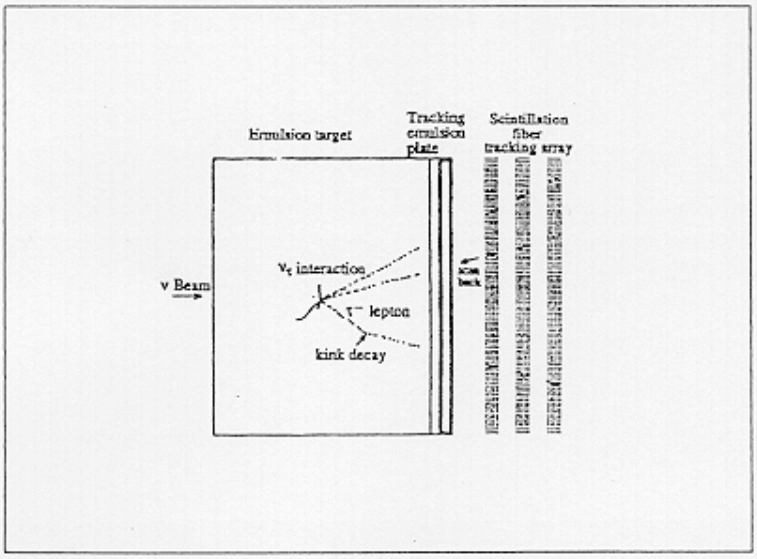

The expected configuration of a typical $\nu_\tau N \rightarrow \tau^- X$ event in the emulsion and scintillating fibre tracker. The average τ^- decay length is ~1mm.

Figure (1-13)

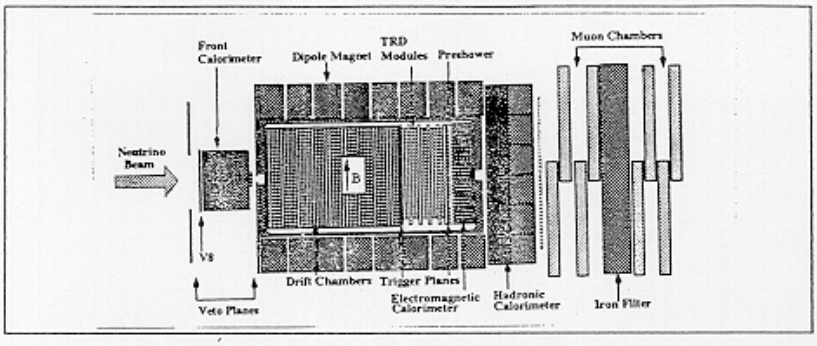

The NOMAD detector (top view).

Figure (1-14)

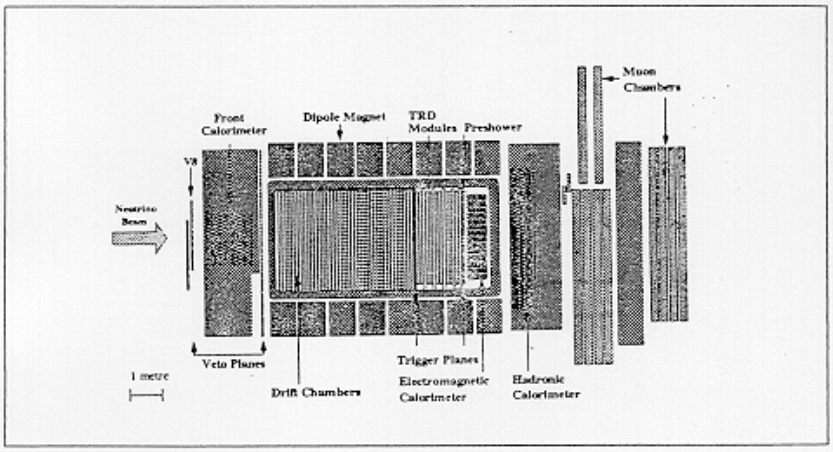

The NOMAD detector (side view).

Figure (1-15)

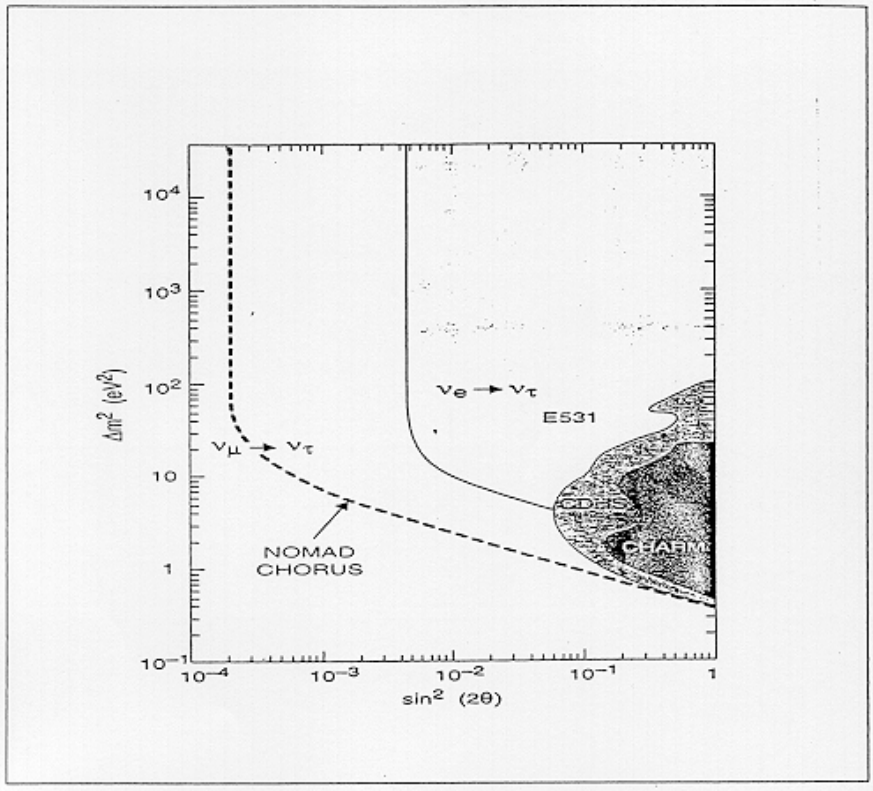

The region of the ($\sin^2 2\theta, \Delta m^2$) plane excluded by the combined CHORUS and NOMAD results if no signal is seen in either experiment. The exclusion regions from previous experiments are also shown.

Figure (1-16)

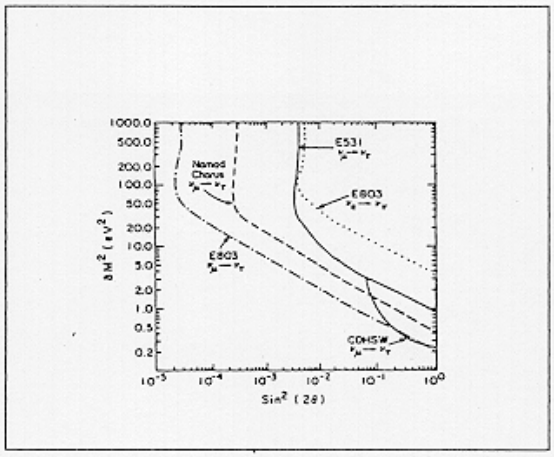

The region of the ($\sin^2 2\theta, \Delta m^2$) plane which will be excluded by COSMOS if no oscillation signal is observed.

Figure (1-17)

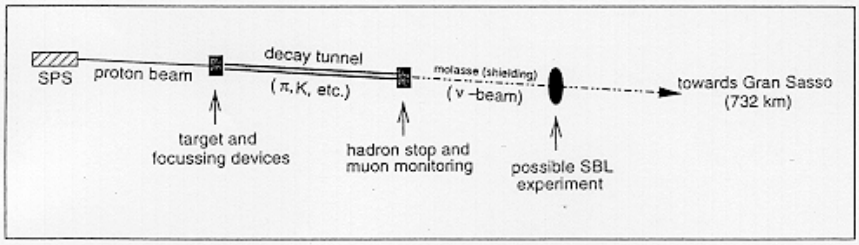

The layout of the CERN to Gran Sasso beam line.

Figure (1-18)

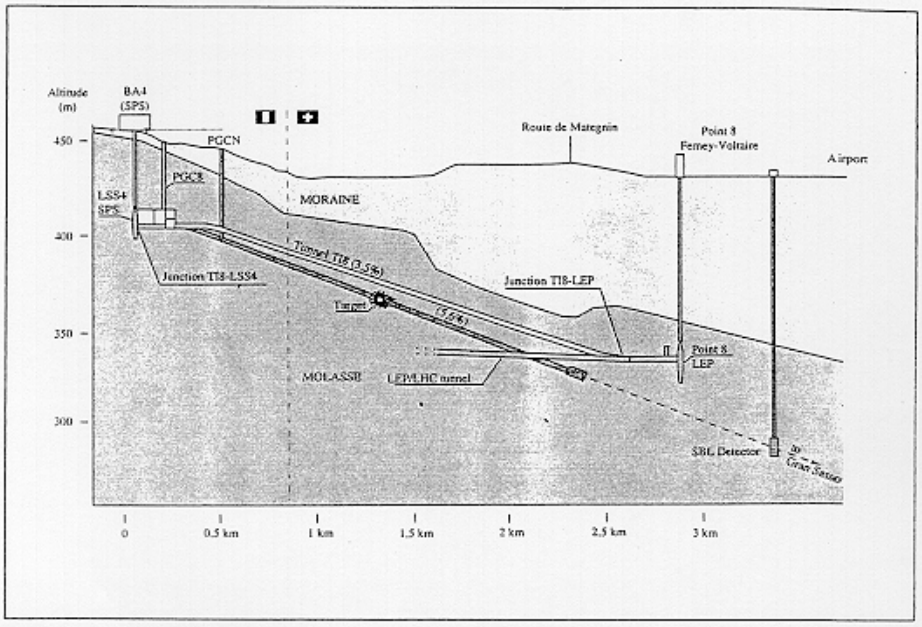

The vertical cut showing the main components of the CERN to Gran Sasso beam line.

Figure (1-19)

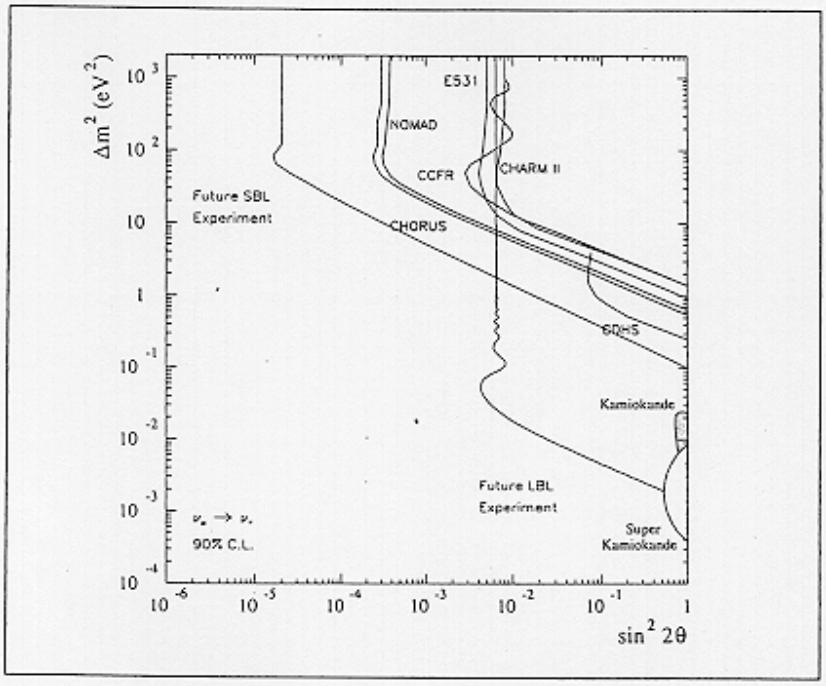

Oscillation parameter range to be covered by future SBL and LBL experiments at the CERN to Gran Sasso neutrino facility.

CHAPTER 2
MAGNETIC HORN AND REFLECTOR

1.GENERAL CHARACTERISTICS.

These elements are 2 pulsed toroidal lenses designed to focus the pions and kaons emitted from the target into a nearly parallel beam. This beam produces muon and neutrino decay products along its path in the rest of the neutrino cave and in the decay tunnel.

1.1 Horn and reflector focusing effect.

The magnetic volume is confined between the inner and outer conductor of the horn or the reflector with the azimuthal magnetic induction B varying as $B = \frac{\mu_0 I}{2\pi r}$ (SI units) .

The current I is of the order of 100 kA for both elements .

In first approximation, the thickness of the inner conductor can be neglected so that the horn and reflector are transparent to the particles. Depending on the polarity of **B**, only the charged particles of one sign are bent by the magnetic field in the right direction and are focused into a nearly parallel beam. The charged particles of the opposite sign are bent in the opposite direction and leave the beam . In the actual neutrino cave, the positive parent particles are the ones focused by the horn-reflector pair (see figure (2-1)).

The reflector has a large central aperture to allow the particles which are already well focused to pass undisturbed, but provides additional focusing for particles of different energies which have not been properly focused by the horn
(see figure (2-2)). In this way the energy band which is focused by the system is broadened.

1.2 General design criteria.

i)The magnetic horn and reflector are optically designed to enhance as much as possible the neutrino flux in the detector volumes of CHORUS and NOMAD and are optimized in terms of inner and outer conductor shape by calculating the trajectories of the neutrino parent particles (pions and kaons).

For example, the horn and reflector which are actually located in the neutrino cave have enhancement factors of 5 and 2 respectively and lead to a neutrino flux peak around 29GeV. The currents chosen to aim at excellent reliability are I_H = 100kA and I_R = 120kA .

Neutrino energy	**Enhancement**	**of neutrino**	**flux**
(GeV)	horn only	reflector only	horn and reflector
29	≈ 5	≈ 2	≈ 10

ii)To achieve good electrical contacts one must keep in mind that contact pressure must not vanish when pulsing. Concerning the horn, the inner conductor is in first approximation forced into traction when pulsed and its length tends to increase. Thus the contact pressure will increase only if the structure (end-plates and outer conductor) is stiff enough .

iii)Precise centering of inner and outer conductor is very important since the electromagnetic forces will tend to pull the conductor into center line, thus creating alternate flexion .

iv)Fatigue effect for10 million alternate tractions must be taken into account on the mechanical stress limit .

v)Natural oscillating frequency of the inner conductor must remain away from the fundamental frequencies of the current pulse .

vi)Symmetry of revolution of the magnetic field distribution has to be as good as possible and especially on the current feeding side of the magnetic volume : one necessary basic condition to that aim is to have the currents in the feeding strip-lines equal .

1.3 Mechanical construction.

The general assemby of the horn station is shown in figure (2-3).

In the mechanical design special care has been taken in order to :

(a)improve the electrical contacts between each conductor and the assembling method.

(b)provide a light, strong and adjustable centering appliance using stainless steel cables to hold and center the inner conductor with respect to the outer conductor.

(c)keep the material thickness of the inner conductor to a minimum to reduce particle absorption loss .

(d)avoid organic insulation material : the use of an adapting pulse power transformer with low voltage on the horn and reflector made it possible to work without using organic insulation materials whose limited life constitutes a critical limiting factor in the high radiation areas .

The inner conductor is made in 4 pieces (see figure (2-4)) and is cooled by spraying continuously water onto it. The outer conductor is cylindrical with inner diameter of 420mm and a wall thickness of 15mm and is made in 5 pieces.

1.4 Pulsed operation mode.

Horn and reflector work in pulsed operation mode by synchronized discharge of a corresponding pulse generator. The horn and reflector current pulses must be synchronized with the extraction of protons from the SPS.

As an illustration, it is useful to see what is actually the case in the WANF :

Two spills of protons of 6 ms duration and 2.7 ms separation are extracted from the SPS (Super Proton Synchrotron) for each machine cycle of 14.4 s (see figure (2-5)). The parameters of the current pulses of the horn and reflector are shown in figures (2-6) and (2-7).

Figure (2-1)

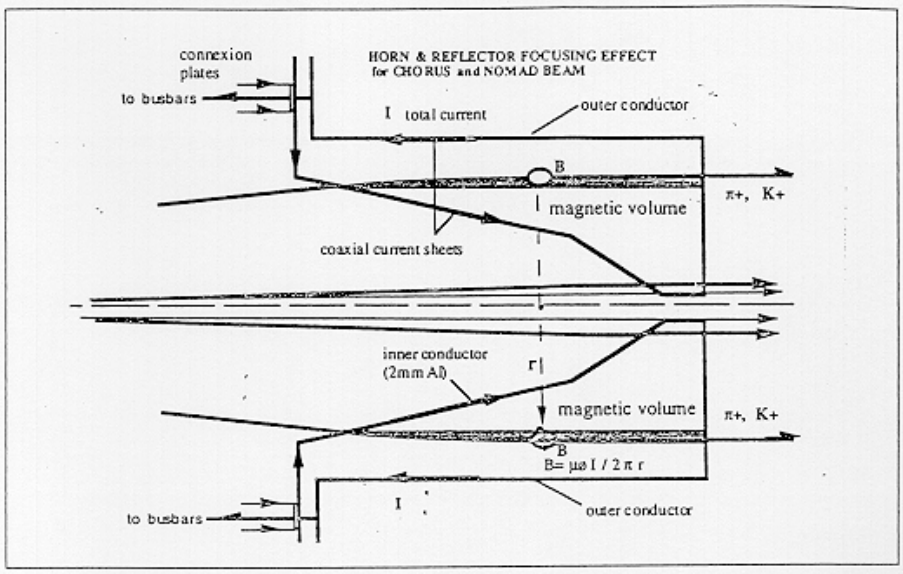

Horn and reflector focusing effect.

Figure (2-2)

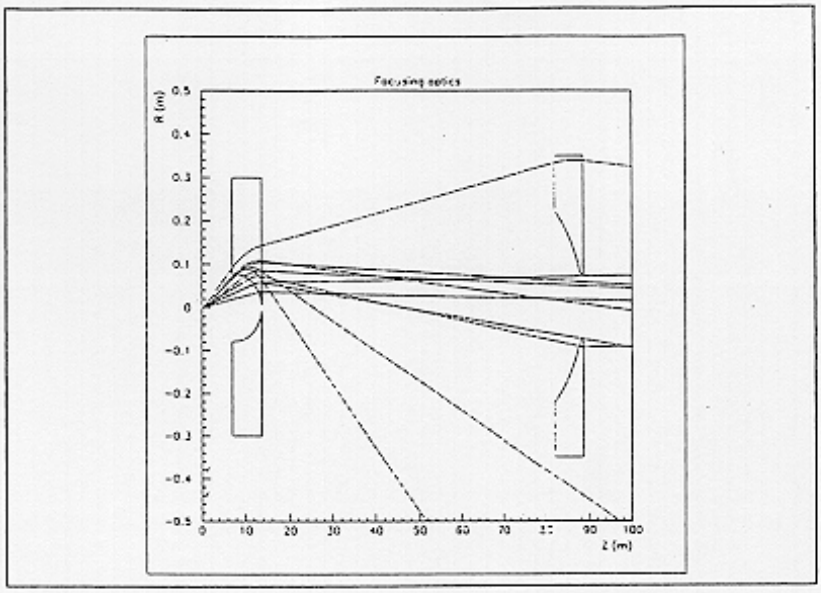

Particles emerging from the target deviated in the fields of horn and reflector.

Figure (2-3)
Neutrino magnetic horn: General assembly.

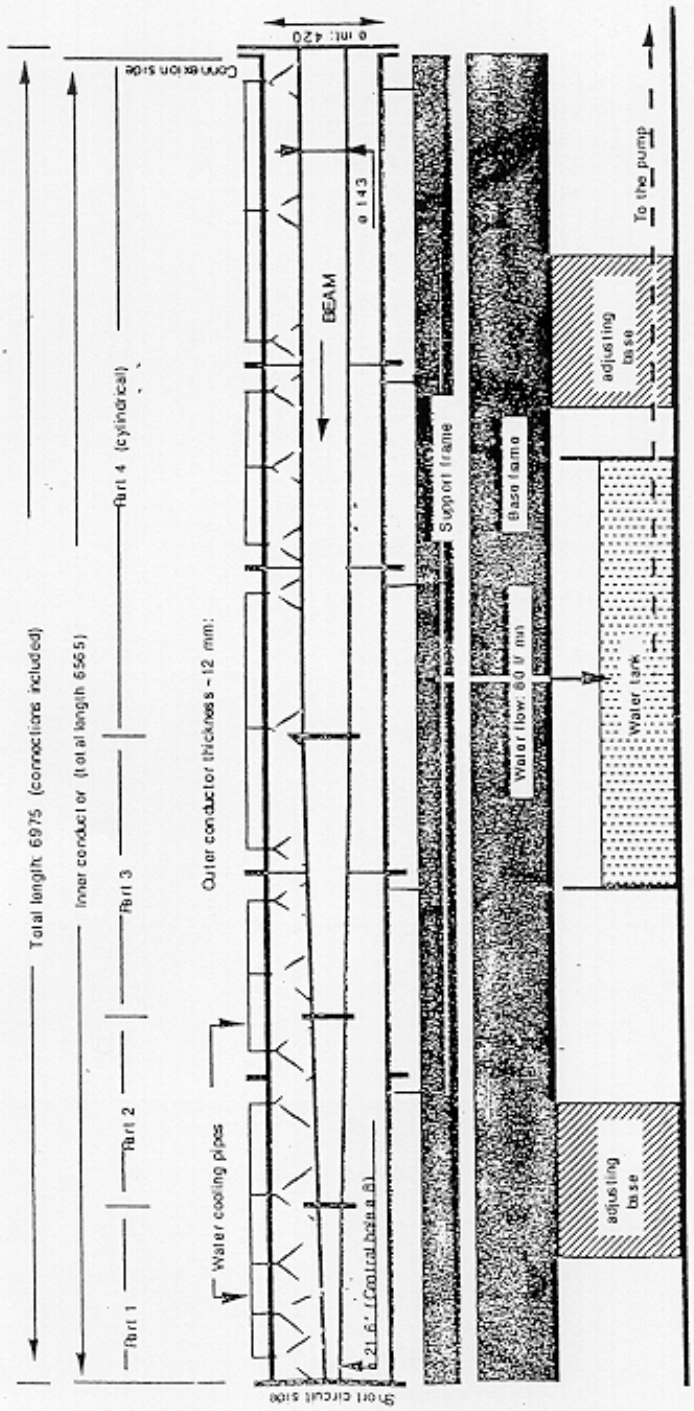

Figure (2-4)
Horn inner conductor.

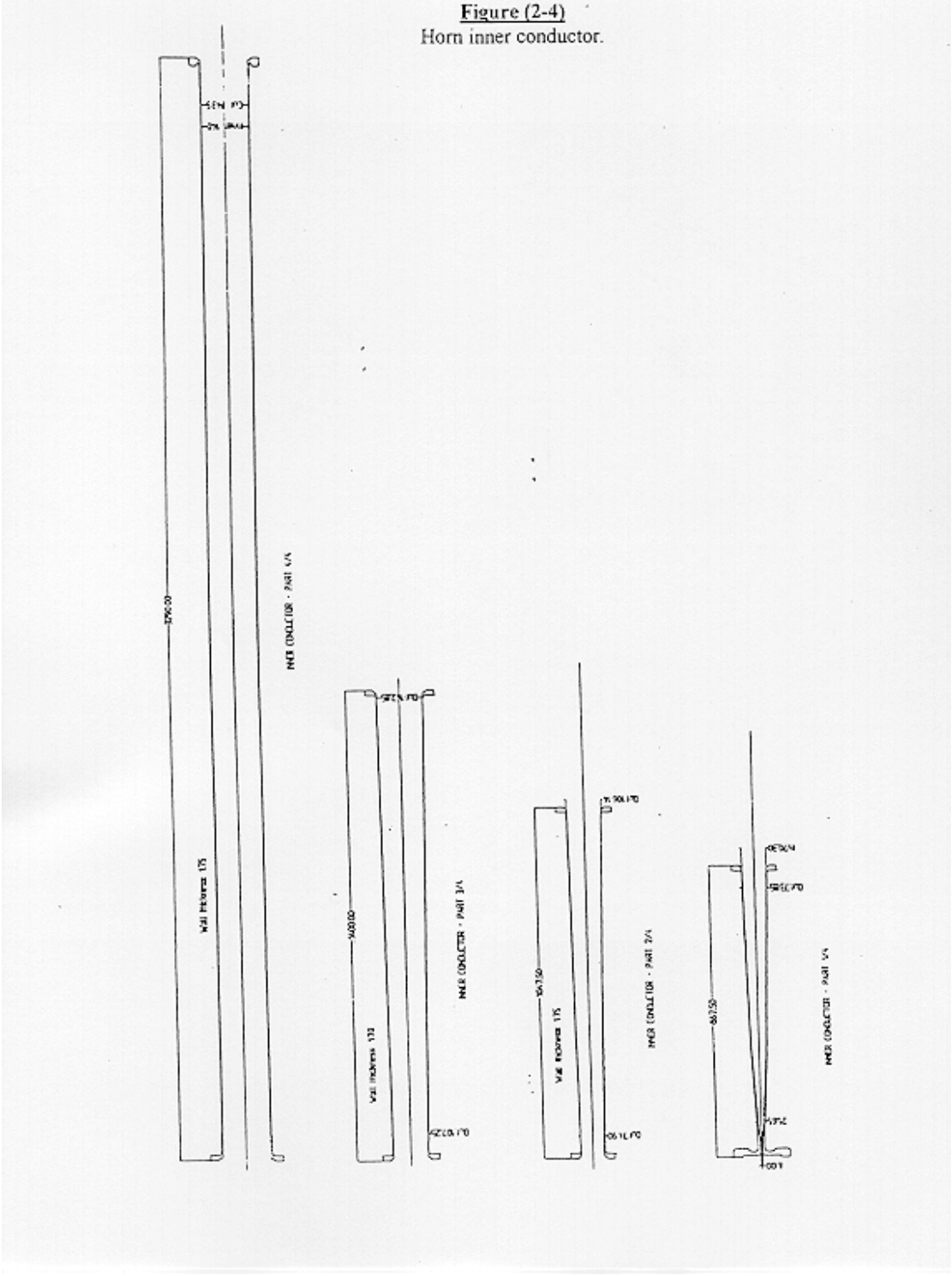

Figure (2-5)

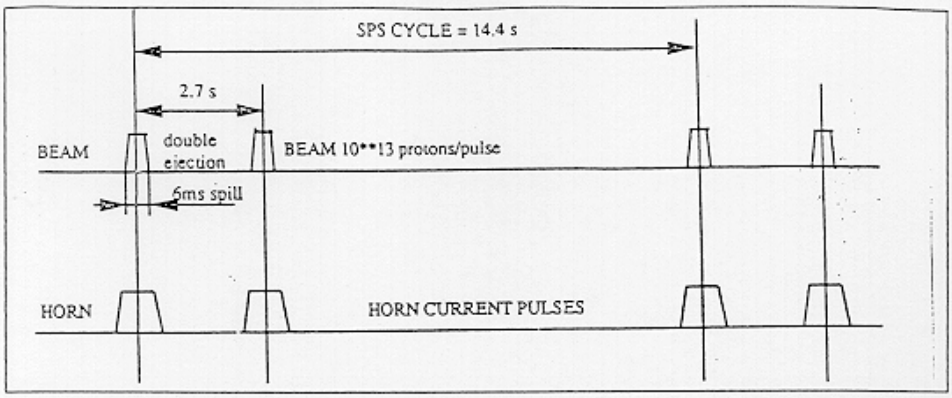

SPS timing sequence.

Figure (2-6)

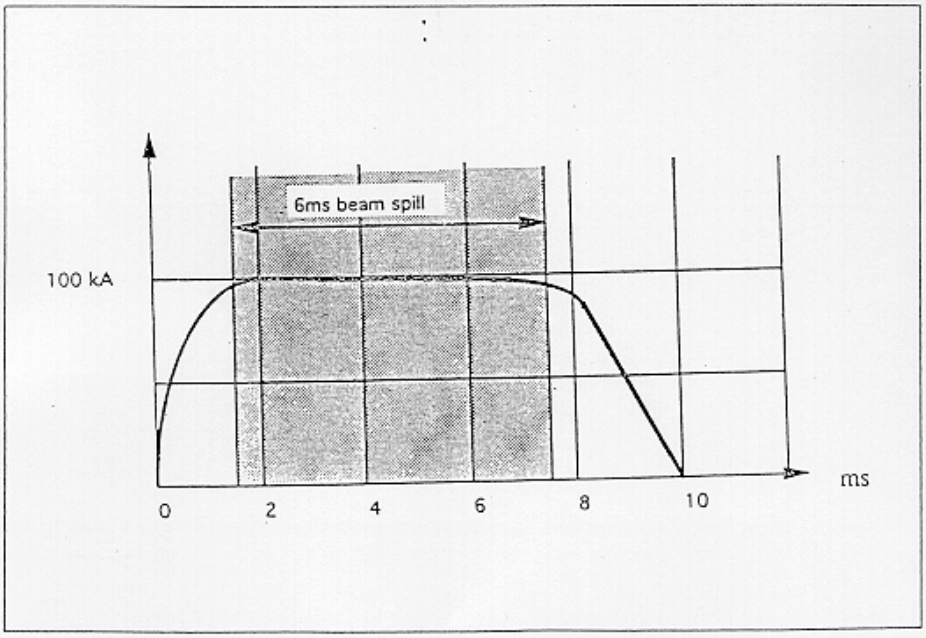

Horn current pulse.

Figure (2-7)

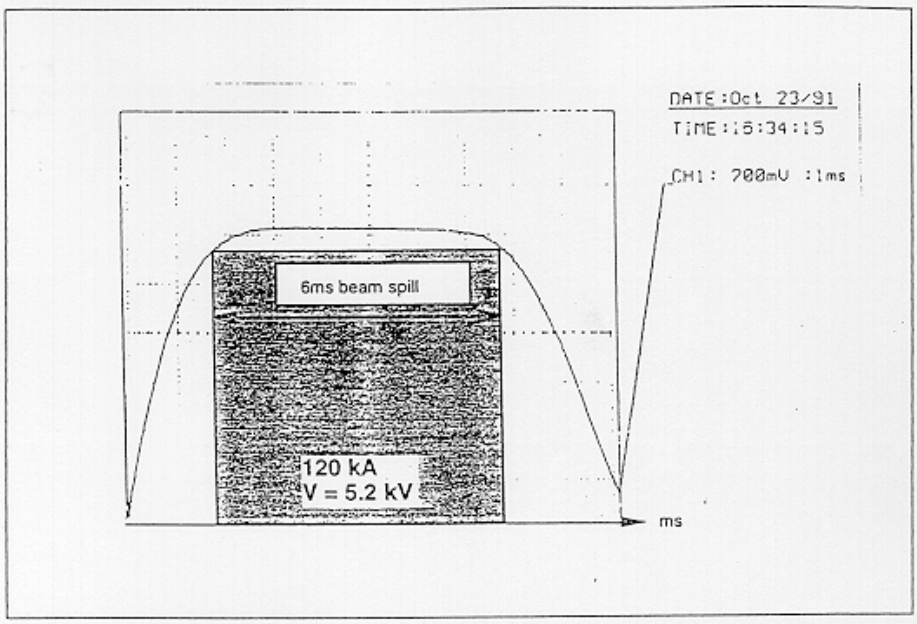

Reflector current pulse.

CHAPTER 3

DESIGN OF THE MAGNETIC HORN

1.GENERAL PURPOSE AND REQUIREMENTS.

The aim was to determine the shape of the inner conductor of a magnetic horn, which would focus a beam of charged particles :

1) of a given momentum p

We concentrated on the momentum range 20-100 GeV/c and especially on momenta around 50 GeV/c, as in the neutrino beam line the π^+ 's of this energy range are the parent particles of interest.

2) of initial emission angle φ

We tried to focus almost perfectly particles with emission angles from -10 mrad to +10 mrad with respect to the axis, as this acceptance is what we have in the actual horn in the neutrino cave. However, in case a larger acceptance is required the results can be easily extended.

3) emitted isotropically from a point source on the horn axis.

The consideration of a point source is quite acceptable as long as the horn is going to be placed at least 20-30 m away from the target .If this is not the case, then additional study is necessary to include the effects due to the dimensions of the source (target). The term "isotropical distribution" means, here, that all emission directions with initial angles $\varphi \in$ [-10mrad,+10mrad] with respect to the z axis are equivalent (no preference for one or another). This assumption is quite useful for a preliminary design, although the distribution of the parent particles emitted by the source is clearly not isotropical and depends on the interactions between the impinging protons and the target material.

In order to do that we first had to fix :

1. the distance D of the end part of the horn from the source of the particles.
2. the current I at which the horn should operate. As a result of technical restrictions, this current cannot be higher than 120 kA .

2.MOTION OF A CHARGED PARTICLE INSIDE THE MAGNETIC FIELD OF THE HORN.

As a first step to determine the geometry of the inner conductor of the horn it was necessary to study the motion of a charged particle in the magnetic field :

$$B = \frac{\mu_0 I}{2\pi r} \qquad (1a) \quad (SI\ units)$$

where I is the current of the horn and r the distance from the axis of the horn .
It is convenient to take a system of cylindrical coordinates (r,θ,z) to describe the motion of a particle of charge e and of momentum p (velocity v) .The particle is emitted from the point source S and its velocity **v** makes an angle φ with the z axis. The particle enters the field at the point A($r = r_0$,$z = 0$) . In order to have he required focusing effect the particle has to leave the field parallel to the z axis at some point C ($r = r_{max}$, $z = z_{max}$) .

The magnetic field is $\mathbf{B} = \frac{\mu_0 I}{2\pi r}\ \mathbf{u_\theta}$ (1b)

The trajectory of the particle lies on the plane Orz, that is the plane defined by S, A and C . So, for the motion of the particle :

$$\theta = const. \Rightarrow \frac{d\theta}{dt} = 0$$

Figure (3-1)

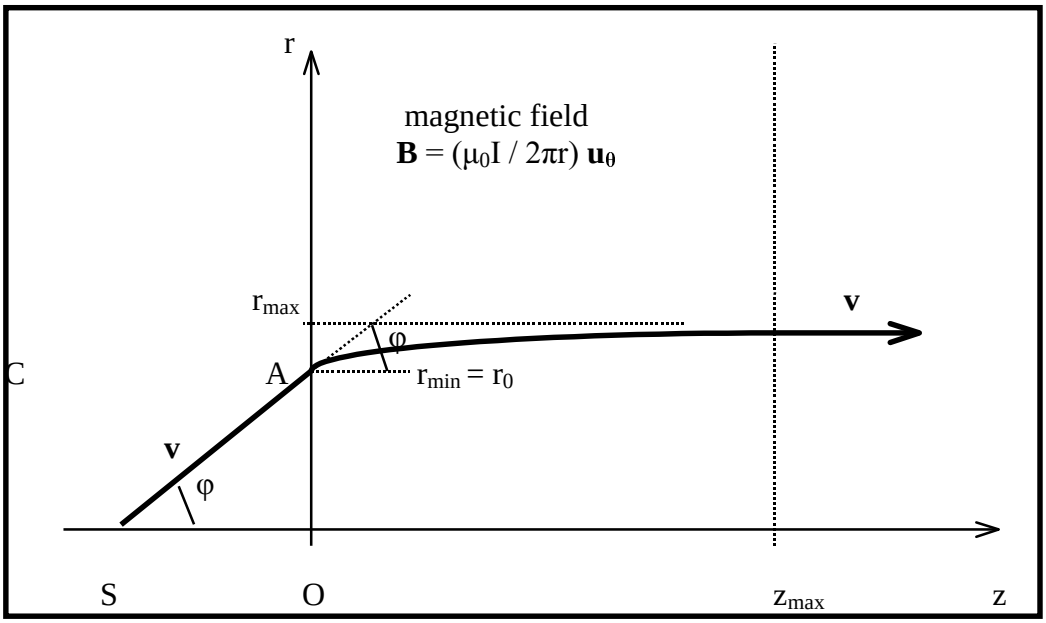

2.1 Equations of motion.

The magnetic force $\mathbf{F} = e\,\mathbf{v}\times\mathbf{B}$ acts on the particle, so the Fundamental law of Dynamics reads : $m\,\mathbf{a} = e\,\mathbf{v}\times\mathbf{B}$ (2)

where $m = \dfrac{m_0}{\sqrt{1-\dfrac{v^2}{c^2}}} = m_0\gamma$ (3) is the relativistic mass of the particle.

After expressing **v** and **a** in cylindrical coordinates by means of the formulas :

$$\mathbf{v} = \frac{dr}{dt}\,\mathbf{u_r} + r\,\frac{d\theta}{dt}\,\mathbf{u_\theta} + \frac{dz}{dt}\,\mathbf{u_z} \qquad (4a)$$

$$\mathbf{a} = \left[\frac{d^2r}{dt^2} - r\left(\frac{d\theta}{dt}\right)^2\right]\mathbf{u_r} + \left(2\frac{dr}{dt}\frac{d\theta}{dt} + r\frac{d^2\theta}{dt^2}\right)\mathbf{u_\theta} + \frac{d^2z}{dt^2}\,\mathbf{u_z} \qquad (4b)$$

and substituting into the Fundamental law of Dynamics, we have the following equations of motion :

$$\frac{d^2r}{dt^2} = -n\frac{dz}{dt}B \qquad (5)$$

$$\frac{d^2z}{dt^2} = n\frac{dr}{dt}B \qquad (6)$$

$$\frac{d}{dt}\left(r^2\frac{d\theta}{dt}\right) = 0 \qquad (7)$$

where $n \equiv \dfrac{e}{m} = \dfrac{e}{m_0\gamma} = \dfrac{ev}{p}$ (8a) in SI units

or $n = \dfrac{vc}{p}$ (8b) with p expressed in eV/c.

Notice that Eq.(7) is automatically satisfied since the trajectory lies on a plane ($d\theta/dt = 0$) .

Furthermore, $\mathbf{v}\bullet\mathbf{a} = n\,\mathbf{v}\bullet(\mathbf{v}\times\mathbf{B}) = 0 \Rightarrow v = \text{const.}$ (9)

2.2 Approximative solutions to the equations of motion.

If the energy of the particle is higher than 100 eV , which is the case since we are dealing with energies between 10 and 100 GeV , Eqs.(5) and (6) have the following approximative solutions [ref. 2]:

$$\frac{dr}{dt} = \pm\sqrt{f(r)} \qquad (10)$$

$$\frac{dz}{dt} = g(r) \qquad (11)$$

The functions f(r) and g(r) are given respectively by the formulas :

$$f(r) \cong v^2\left(b^2 - A\ln\frac{r}{r_0}\right) \qquad (12)$$

$$g(r) \cong v \qquad (13)$$

$$b \equiv \tan\phi \qquad (14)$$

$$A \equiv \frac{\mu_0 cI}{\pi p} \qquad (15)$$ where p is in eV/c.

So, we have

$$\frac{dr}{dt} \cong \pm v\sqrt{b^2 - A\ln\frac{r}{r_0}} \qquad (16)$$

$$\frac{dz}{dt} \cong v \qquad (17)$$

Notice that the last equation means that the projection of the motion on the z axis is almost uniform.

Combining the formulas above we have the equation :

$$\frac{dr}{dz} \cong \pm\sqrt{b^2 - A\ln\frac{r}{r_0}} \qquad (18)$$

which relates the slope of the trajectory at any point (r,z) to the parameters A,b and r_0.

Calculation of r_{max} .

In order to calculate r_{max} we notice that it is the root of the equation

$$\frac{dr}{dt} = 0 \Rightarrow f(r) = 0$$ and we finally have $r_{max} = r_0 \exp\left(\frac{b^2}{A}\right)$ (19) .

Restrictions on r_0 and r_{max} .

We must obviously have $r_0 > R_{in}$ and $r_{max} < R_{out}$ where R_{in} is the radius of the inner conductor of the horn and R_{out} is the radius of the outer conductor of the horn . R_{in} and R_{out} are both determined by technical/engineering restrictions.

Boundary conditions.

The initial direction of the momentum makes an angle φ with the z axis and the particle should leave the magnetic field with its momentum parallel to the z axis. Eq.(18) must then be solved according to the boundary conditions :

$$\frac{dr}{dz} = b \equiv \tan\phi \qquad \text{at point A}(r = r_0 , z = 0) \qquad (20a)$$

$$\frac{dr}{dz} = 0 \qquad \text{at point C}(r = r_{max} , z = z_{max}) \qquad (20b)$$

Calculation of z_{max} .

In Eq.(18) there is ± .Since, on physical grounds, it is obviously expected that for the shape of the horn (dr/dz) > 0 only the sign + is acceptable. Thus :

$$dz = \frac{dr}{\sqrt{b^2 - A\ln\frac{r}{r_0}}} \qquad (21)$$

Integrating between points A($r = r_0 , z = 0$) and C($r = r_{max} , z = z_{max}$) and setting

$u \equiv \frac{r}{r_0}$ (22) we have :

$$z_{max} - z = r_0 \int_{\frac{r}{r_0}}^{\frac{r_{max}}{r_0}} \frac{du}{\sqrt{b^2 - A\ln u}} \qquad (23)$$

For the coordinates of the point A($r = r_0 , z = 0$) Eq.(23) gives :

$$z_{max} = r_0 \int_{1}^{\frac{r_{max}}{r_0}} \frac{du}{\sqrt{b^2 - A\ln u}} \qquad (24)$$

We introduce now the variable $w \equiv \sqrt{\frac{b^2 - A\ln u}{A}}$ (25) and using Eq.(19) we have

$$z_{\max} = \frac{2}{\sqrt{A}} r_0 \exp(x^2) \int_0^x \exp(-w^2) dw = r_0 \sqrt{\frac{\pi}{A}} \exp(x^2) erf(x) \qquad (26)$$ where

$$x \equiv \frac{b}{\sqrt{A}} \quad (27)$$ and by definition $$erf(x) \equiv \frac{2}{\sqrt{\pi}} \int_0^x \exp(-w^2) dw \qquad (28a)$$

The error function erf(x) can be represented by an alternating power series :

$$erf(x) = \frac{2x}{\sqrt{\pi}} \left[1 - \frac{x^2}{1!3} + \frac{x^4}{2!5} - \frac{x^6}{3!7} + ... \right] \qquad (28b)$$

Thus we have :

$$z_{\max} = \frac{2}{\sqrt{A}} r_0 e^{x^2} x \left[1 - \frac{x^2}{1!3} + \frac{x^4}{2!5} - \frac{x^6}{3!7} + ... \right] = r_0 u(b, A) \qquad (29)$$

where $$u(b, A) \equiv \frac{2}{\sqrt{A}} e^{x^2} x \left[1 - \frac{x^2}{1!3} + \frac{x^4}{2!5} - \frac{x^6}{3!7} + ... \right] \quad (30)$$ is a function of b and A since

$$x \equiv \frac{b}{\sqrt{A}} \ .$$

Eq.(29) gives the value of z_{max} in terms of r_0 ,p,I and φ ,since A and x are completely determined by p,I and φ through Eqs.(14), (15) and (27) .

3.PROCEDURE FOR DETERMINING THE SHAPE OF THE INNER CONDUCTOR.

3.1 Computational scheme.

The shape of the inner conductor can now be determined since z_{max} is actually the length of the magnetic field required, if a particle with parameters p,φ and r_0 is to leave the horn parallel to the z axis. We set $L \equiv z_{max}$ (31) .

The computational scheme is the following :

1)We fix the parameters p (particle momentum) , I (current) and D ≡ (SP) .Then A is calculated by means of Eq.(15).

2)We choose an angle φ ∈ [0 mrad, 10 mrad] .Then b ≡ tanφ≅φ , since φ very small .

3)We set $$d \equiv \frac{r_0}{\tan\phi} \cong \frac{r_0}{\phi} \quad (32)$$; d measures the projection of SA on the z axis. From the geometry we have d + L = D (33) .

4)Furthermore, it is $L = r_0 u(b,A)$. Since b and A are known u(b,A) can be calculated by means of Eq.(30) .

Remark : As $x = \frac{b}{\sqrt{A}} \cong \frac{\phi}{\sqrt{A}}$ (34) and φ is small x is also quite small and only the first terms in the series appearing in u(b,A) are important.

5)Then, $\frac{r_0}{\phi} + r_0 u(b, A) = D \Rightarrow r_0 = \frac{D}{\frac{1}{\phi} + u(b, A)}$ (35) ; hence, r_0 is determined .

6)Then, r_{max} is determined from $r_{max} = r_0 \exp\left(\frac{b^2}{A}\right)$

7)Finally, L is determined from $L = D - \frac{r_0}{\phi}$ (36) .

8)Taking S (the source) to be the origin of our system of cylindrical coordinates, the previous steps determine the points A(r_0,d) and C(r_{max} , D) as well as the length of the field L.

9)Repeating the calculation for different values of φ we find the points A1, C1,A2,C2,A3,C3..., which define the shape of the inner conductor. Obviously, for φ ∈ [-10 mrad, 0 mrad] the shape of the inner conductor is just the symmetrical with respect to the z axis .

Figure (3-2)

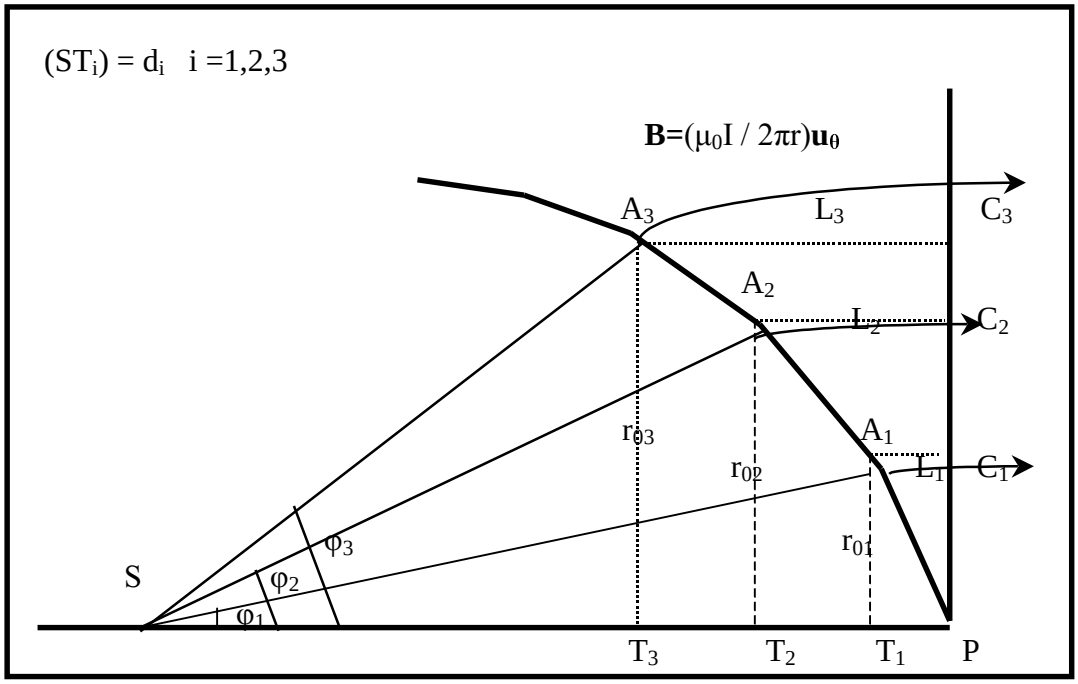

3.2 An elegant approximative formula.

In our case, I ~100 kA = 10^5 A, p ~10 GeV/c and φ ~1mrad = 10^{-3} rad (see part 1).

Then, $A = \frac{\mu_0 cI}{\pi p} \sim \frac{4\times 10^{-7}\cdot 3\times 10^{8}\cdot 10^{5}}{314\cdot 10^{10}} \sim 10^{-4}$ and $x = \frac{b}{\sqrt{A}} \cong \frac{\phi}{\sqrt{\eta}} \sim$

$$\frac{10^{-3}}{\sqrt{10^{-4}}} = 10^{-1}$$

Thus, $x^2 \sim 10^{-2}$ and we can make the following approximations :

$$e^{x^2} \cong 1 + x^2 \qquad (37)$$

$$1 - \frac{x^2}{1!3} + \frac{x^4}{2!5} - \frac{x^6}{3!7} + .. \cong 1 - \frac{x^2}{3} \qquad (38)$$

Finally, using Eqs.(29),(31),(34),(37) and (38) we have

$$L \cong r_0 \frac{2}{A}\phi\left(1 + \frac{2}{3}\frac{\phi^2}{A}\right) \qquad (39)$$

From Eq.(35) we have $r_0 = (D - L)\phi$ and substituting in Eq.(39) and solving for L we have

$$L = \frac{D\phi^2 k}{\frac{A}{2} + \phi^2 k} \quad (40a) \quad \text{where } k \equiv 1 + \frac{2}{3}\frac{\phi^2}{A} \quad (40b).$$

Since $\mu_0 = 4\pi\times10^{-7}$ N/A^2 and c=3×10^8 m/sec : $\mu_0 c = 120\pi$ JA^{-2}sec^{-1} and we can write

$$A = 120\frac{I}{p} \quad (41) \quad \text{with p in eV/c.}$$

Finally :

$$L = \frac{Dp\phi^2 k}{60I + p\phi^2 k} \qquad k \equiv 1 + \frac{1}{180}\frac{p\phi^2}{I} \qquad (42)$$

where :		or
p particle momentum	[eV/c]	[GeV/c]
φ initial angle with the horn axis	[rad]	[mrad]
I current at the horn	[A]	[kA]
D distance target-end part of the horn	[m]	[m]
L length of the magnetic field in the horn	[m]	[m]

An empirical formula permitting to determine the shape of the inner conductor for φ of the order of a few mrads has been proposed by A.Ball :

$$L = \frac{DE\phi^2}{60I + kE\phi^2} \qquad k \cong 0.625$$

where

E ≅ p [GeV/c]		beam energy
φ	[mrad]	ray angle
I	[kA]	current at the horn
D	[m]	distance target-end part of the horn
L	[m]	field length

Ball's formula works very well and has been the basis for the construction of horns and reflectors at CERN.

The similarity between formula (42),which has been derived from first principles and A.Ball's empirical formula is obvious. Application of both formulas has given very close / practically identical results.

3.3 Examples.

(a)Figure (3-3) :

Horn designed with parameters p = 40GeV/c , D = 10m and I = 100kA.

(b)Figure (3-4) :

Horn designed with parameters p = 40GeV/c , D = 20m and I = 50kA.

(c)Figure (3-5) :

Horn designed with parameters p = 40GeV/c , D = 20m and I = 80kA.

(d)Figure (3-6) :

Horn designed with parameters p = 40GeV/c , D = 20m and I = 100kA.

Figure (3-3)

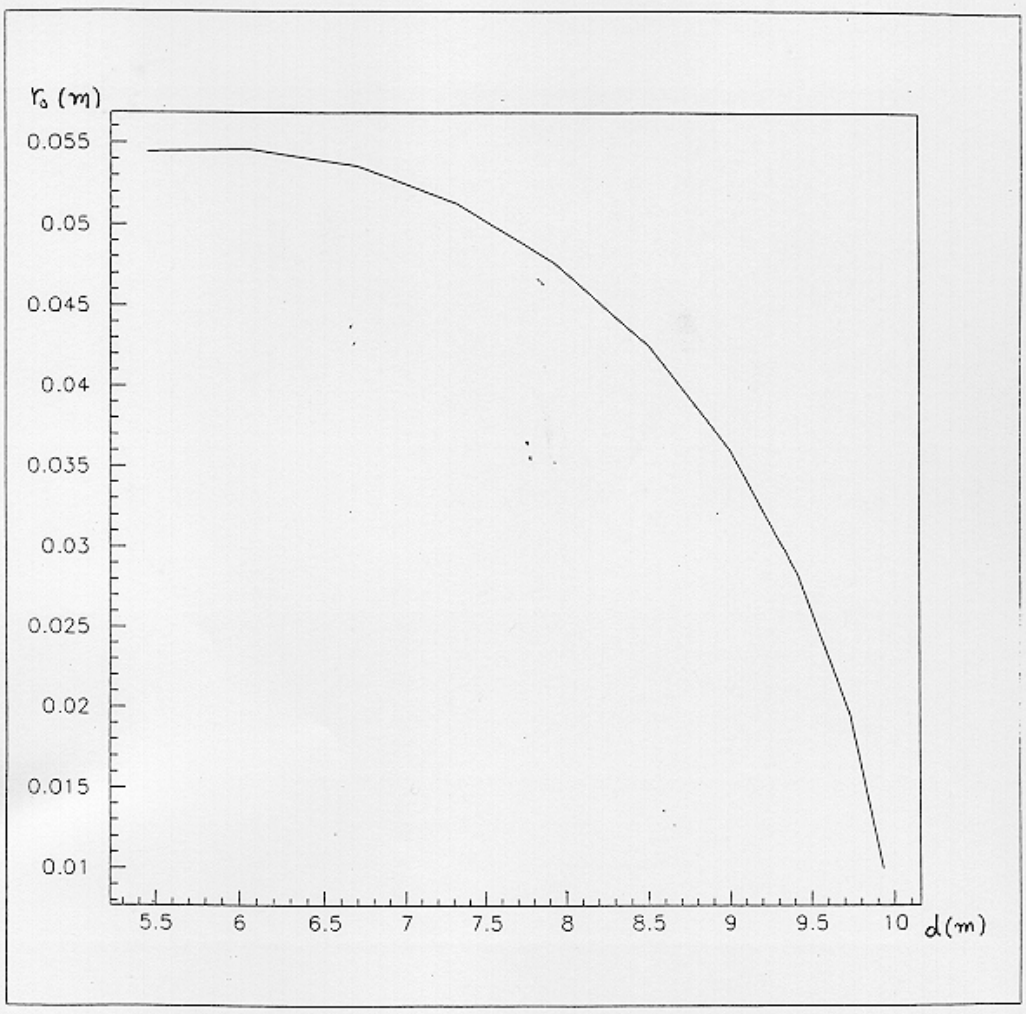

Horn designed with parameters p = 40GeV/c , D = 10m and I = 100kA.

Figure (3-4)

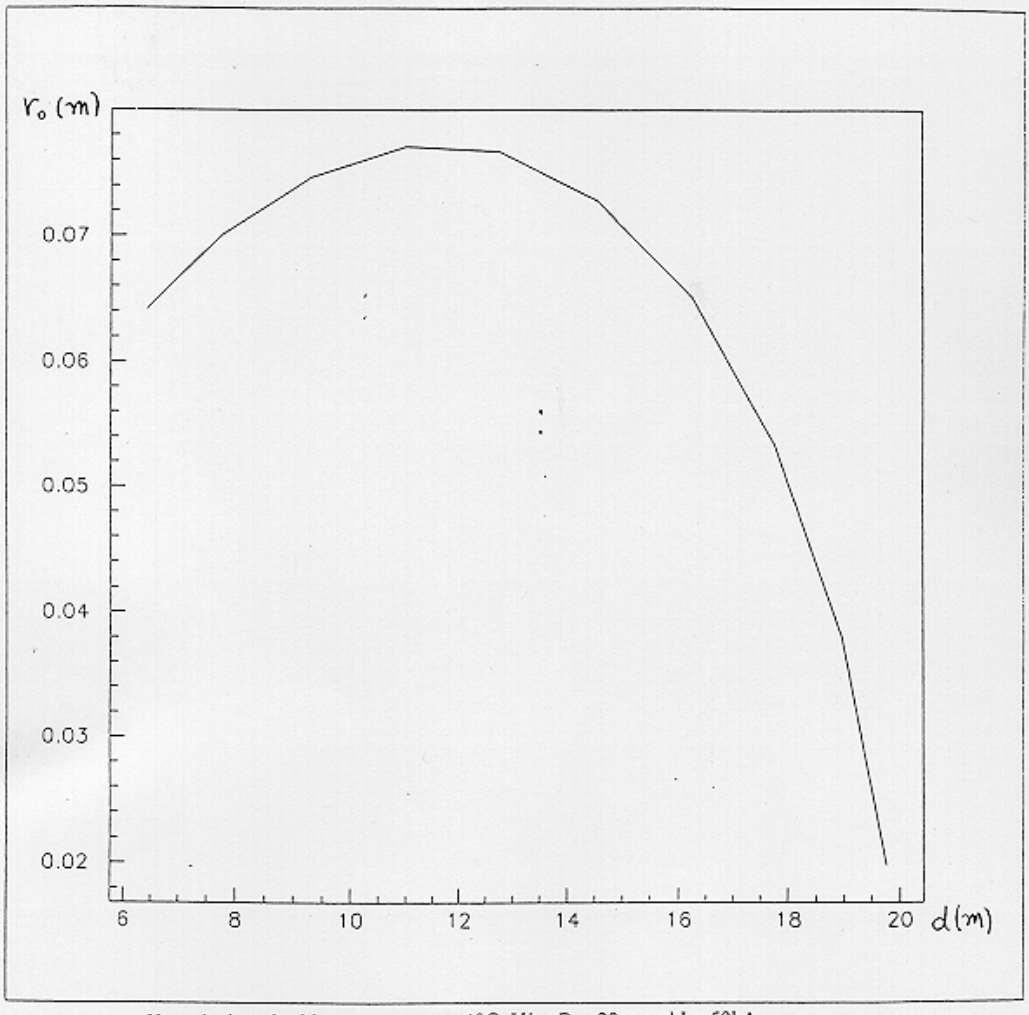

Horn designed with parameters p = 40GeV/c , D = 20m and I = 50kA.

Figure (3-5)

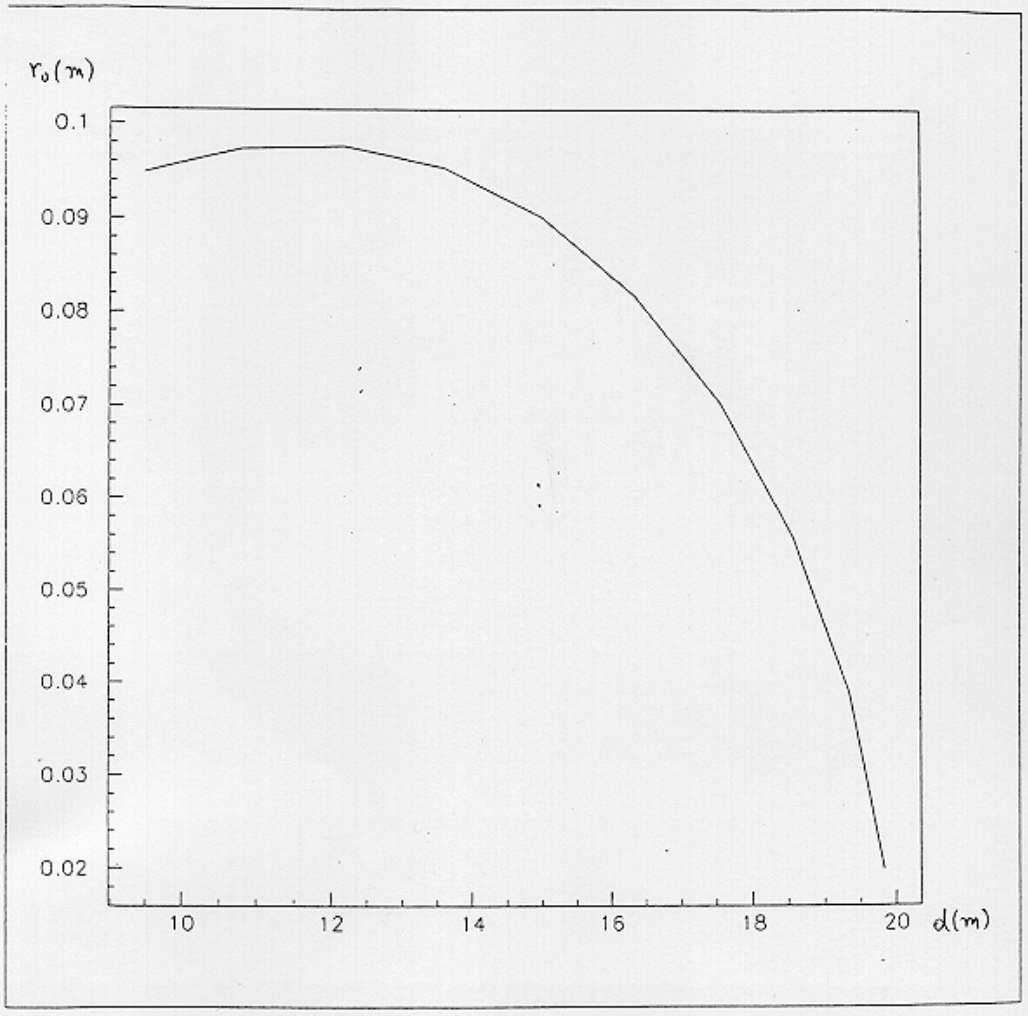

Horn designed with parameters p = 40GeV/c , D = 20m and I = 80kA.

Figure (3-6)

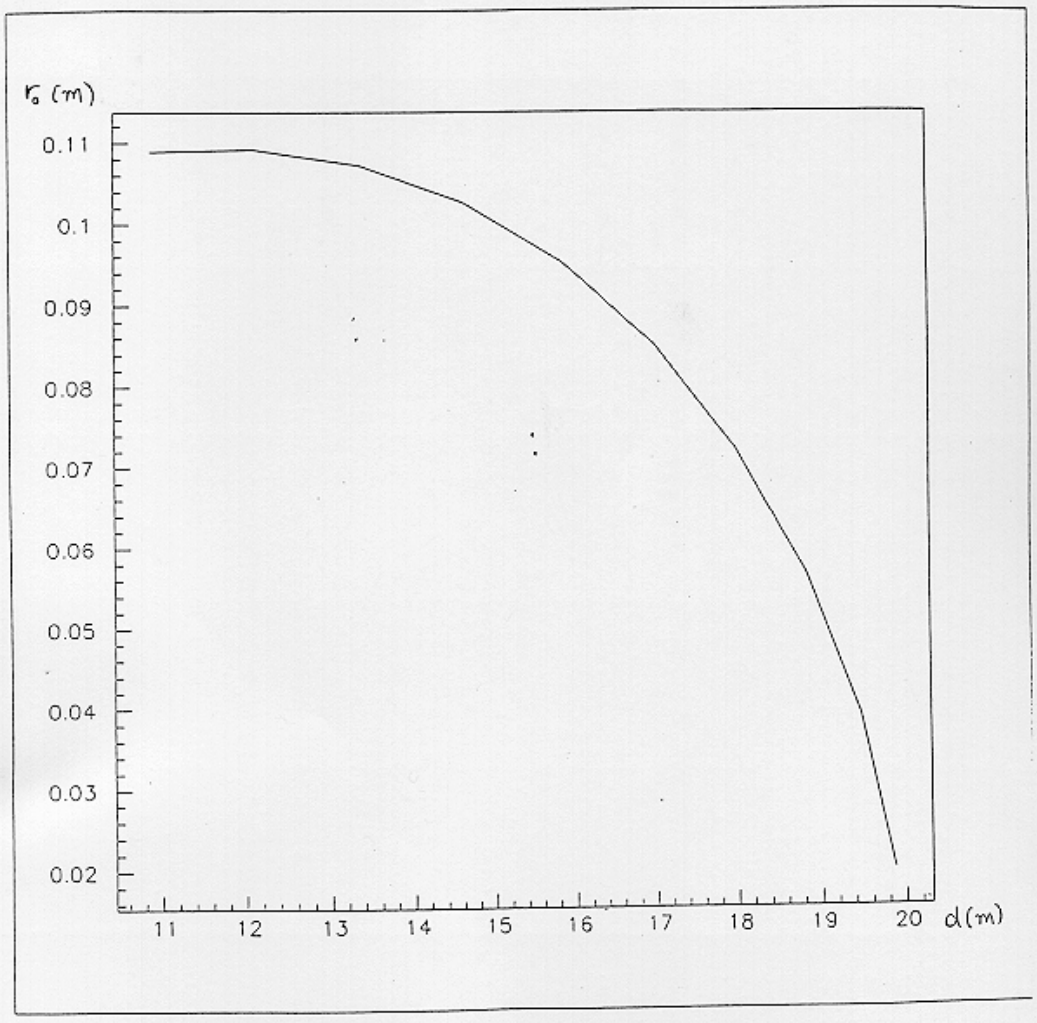

Horn designed with parameters p = 40GeV/c , D = 20m and I = 100kA.

CHAPTER 4

DESIGN OF THE REFLECTOR

The horn is designed to focus particles of a given momentum p_H. Then, the trajectory of a particle with momentum $p \neq p_H$ is bent by in the magnetic field of the horn but does not become parallel to the z axis. If $p > p_H$ the particle is "underfocused" (see figure (4-1)) while if $p < p_H$ the particle is "overfocused" (see figure (4-2)).

1. REFLECTOR REQUIRED TO FOCUS PARTICLES UNDERFOCUSED BY THE HORN.

We consider a particle of momentum $p > p_H$, emitted from the point source S. The initial direction of the particle makes an angle φ with respect to the z axis. The horn is fixed with parameters p_H , I_H (current) and D_H (distance SP) .Taking S as the origin of the coordinate system the particle enters the horn at the point $A(r_{0H} , d_H)$ and leaves the horn at the point $C(r_f , D_H)$, making an angle α $(0< \alpha < \varphi)$ with the z axis. Afterwards the particle enters the reflector and it should leave the reflector parallel to the z axis. The fixed parameters of the reflector are : p(momentum), I_R (current) and D_R (distance of the end part of the reflector from the source S) .

The computational scheme is the following :

1)We take an angle $\varphi \in$ [0 mrad, 10 mrad] .Then $b \equiv \tan\varphi \cong \varphi$.

2)Since the horn is fixed $A_H = \frac{\mu_0 c I_H}{\pi p}$ is known. Then r_{0H} and L_H are determined using either Eqs.(3-35) and (3-36) or Eq.(3-42) and (3-36) .

3) *Calculation of α.*

Eq.(3-18) is in this case (only + is acceptable) : $dz = \frac{dr}{\sqrt{b^2 - A_H \ln \frac{r}{r_{0H}}}}$.

Integrating between points $A(r = r_{0H} , z = d_H)$ and $C(r = r_f, z = D_H)$ we have :

$$L_H = \int_{r_{0H}}^{r_f} \frac{dr}{\sqrt{b^2 - A_H \ln \frac{r}{r_{0H}}}} = r_{0H}\sqrt{\frac{\pi}{A_H}} \exp(x^2)[erf(x) - erf(y)] \qquad (1)$$

where $x \equiv \frac{b}{\sqrt{A_H}}$ (2a) and $y \equiv \frac{\sqrt{b^2 - A_H \ln \frac{r_f}{r_{0H}}}}{\sqrt{A_H}} = \frac{1}{\sqrt{A_H}} \frac{dr}{dz}\Big|_C = \frac{\tan\alpha}{\sqrt{A_H}}$ (3a)

Since φ and α are small we have :

$x \cong \frac{\phi}{\sqrt{A_H}}$ (2b) and $y \cong \frac{\alpha}{\sqrt{A_H}}$ (3b) .

We express the error functions erf(x) and erf(y) as power series of x and y respectively. As in the case of the horn, x, y ~10^{-1} and thus the terms of 4th or higher order in x,y are negligible. Then Eq.(1) becomes :

$$L_H = r_{0H} \frac{2}{\sqrt{A_H}} e^{x^2} \left[x(1 - \frac{x^2}{3}) - y(1 - \frac{y^2}{3}) \right] \qquad (4)$$

Solving for $a \cong y\sqrt{A_H}$:

$$a - \frac{a^3}{3A_H} = \sqrt{A_H} \left[x(1 - \frac{x^2}{3}) - \frac{L_H \sqrt{A_H}}{2r_{0H}} \exp(-x^2) \right] \qquad (5)$$

Eq.(5) can be solved numerically for α .

An interesting special case is when $a >> \frac{a^3}{3A_H}$; then, α is given directly by Eq.(5).

4)*Reflector shape.*

As we can see in figure (4-1), in order to determine the shape of the inner conductor of the reflector we only need to make the substitutions :

HORN		REFLECTOR
φ	↔	α
D_H	↔	$D_R - D_H + \frac{r_{0H}}{\alpha}$
p_H	↔	$p > p_H$

and apply the procedure for the horn or the approximative formula (3-42).
For example, formula (3-42) becomes

$$L_R = \frac{(D_R - D_H + \frac{r_{0H}}{a}) p a^2 k_R}{60 I_R + p a^2 k_R} \quad , \quad k_R = 1 + \frac{1}{180} \frac{p a^2}{I_R}$$

where $r_{0H} = (D_H - L_H)\varphi$ and L_R is the length of the magnetic field inside the reflector.

2. REFLECTOR REQUIRED TO FOCUS PARTICLES OVERFOCUSED BY THE HORN.

We consider a particle of momentum $p < p_H$, emitted from the point source S. The initial direction of the particle makes an angle φ with respect to the z axis. The horn is fixed with parameters p_H, I_H and D_H .Taking S as the origin of the coordinate system the particle enters the horn at the point $A(r_{0H}, d_H)$ and leaves the horn at the point $C(r_f , D_H)$, making an angle β (the angle is negative and β is its absolute value) with the z axis. Afterwards the particle enters the reflector and it should leave the reflector parallel to the z axis. The fixed parameters of the reflector are : p, I_R and D_R .

The computational scheme is the following :

1)We take an angle $\varphi \in$ [0 mrad,10 mrad] .Then $b \equiv \tan\varphi \cong \varphi$.

2)Since the horn is fixed A_H , r_{0H} and L_H are determined as in **1**.

3)*Calculation of β.*

Eq.(3-18) is in this case : $$dz = \begin{cases} + \dfrac{dr}{\sqrt{b^2 - A_H \ln \dfrac{r}{r_{0H}}}}, r_{0H} \le r \le r_1 \\ - \dfrac{dr}{\sqrt{b^2 - A_H \ln \dfrac{r}{r_{0H}}}}, r_f \le r \le r_1 \end{cases} \qquad (6)$$

where r_1 is the maximum distance of the particle from the axis, that is the distance r_{max} for a horn designed to focus particles of momentum p : $r_1 = r_{0H} \exp(\frac{b^2}{A_H})$ (7).

In the same way we set L_1 to be the length of the magnetic field for a horn designed to focus particles of momentum p : $L_1 \equiv \int_{r_{0H}}^{r_1} \frac{dr}{\sqrt{b^2 - A_H \ln \frac{r}{r_{0H}}}}$ (8) .

Obviously, L_1 can be determined by applying the procedure for the horn or the approximative formula (3-42) with parameters p,φ, I_H, D_H .

Integration of (6) gives :

$$L_H = L_1 + \int_{r_f}^{r_1} \frac{dr}{\sqrt{b^2 - A_H \ln \frac{r}{r_{0H}}}} \cong L_1 + r_{0H} \frac{2}{\sqrt{A}} e^{x^2} q(1 - \frac{q^2}{3}) \qquad (9)$$

(we also made the appropriate approximation)

where $x \equiv \frac{b}{\sqrt{A_H}} \cong \frac{\phi}{\sqrt{A_H}}$ (10a) and

$$q \equiv \frac{\sqrt{b^2 - A_H \ln \frac{r_f}{r_{0H}}}}{\sqrt{A_H}} = \frac{1}{\sqrt{A_H}} \frac{dr}{dz} \Big|_C = \frac{\tan \beta}{\sqrt{A_H}} \cong \frac{\beta}{\sqrt{A_H}} \qquad (10b)$$

Solving for $\beta = q\sqrt{A_H}$:

$$\beta - \frac{\beta^3}{3A_H} = A_H \frac{(L_H - L_1)}{2r_{0H}} \exp(-x^2) \qquad (11)$$

Eq.(11) can be solved numerically for β.

An interesting case is when $\beta >> \frac{\beta^3}{3A_H}$; then β is given directly by Eq.(11).

4)*Calculation of r_f.*

From Eq.(10b) we have :

$$\sqrt{b^2 - A_H \ln \frac{r_f}{r_{0H}}} = \tan\beta \cong \beta \Rightarrow r_f = r_{0H} \exp\left(\frac{b^2 - \beta^2}{A_H}\right) \cong r_{0H} \exp\left(\frac{\phi^2 - \beta^2}{A_H}\right) \quad (12)$$

hence r_f is determined.

5)*Reflector shape.*

As we can see in figure (4-2), in order to determine the shape of the inner conductor of the reflector we only need to make the substitutions :

HORN		REFLECTOR
φ	↔	β
D_H	↔	$D_R - D_H - \frac{r_f}{\beta}$
p_H	↔	$p < p_H$

and apply the procedure for the horn or the approximative formula (3-42).

3.EXAMPLES.

(a) Figure (4-3) :

Reflector designed with parameters p = 100 GeV/c , D_R =90m and I_R =120kA.

(b) Figure (4-4) :

Reflector designed with parameters p = 20 GeV/c , D_R =90m and I_R =120kA.

In both cases the horn is designed with parameters p_H = 40GeV/c , D_H = 20m and I_H=100kA.

Figure (4-1)

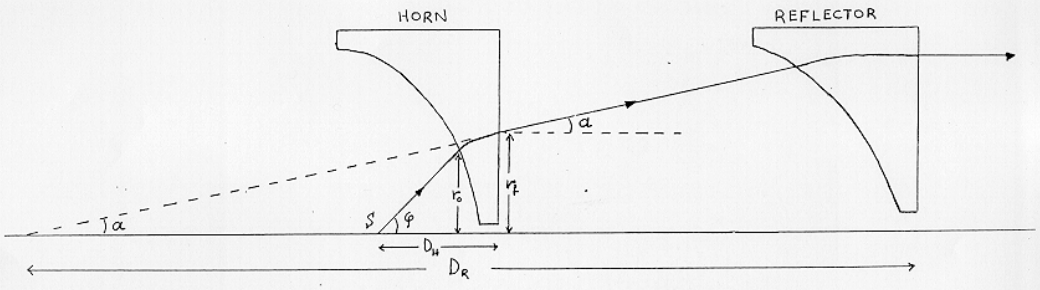

Reflector designed to focus particles underfocused by the horn.

Figure (4-2)

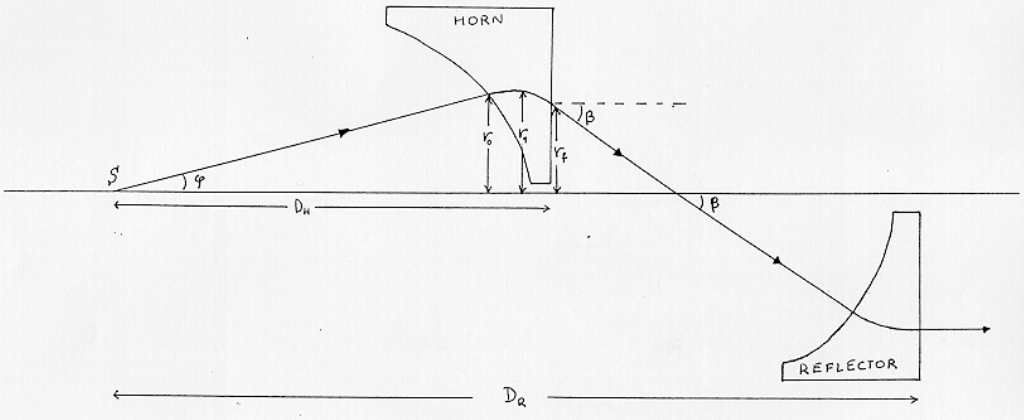

Reflector designed to focus particles overfocused by the horn.

Figure (4-3)

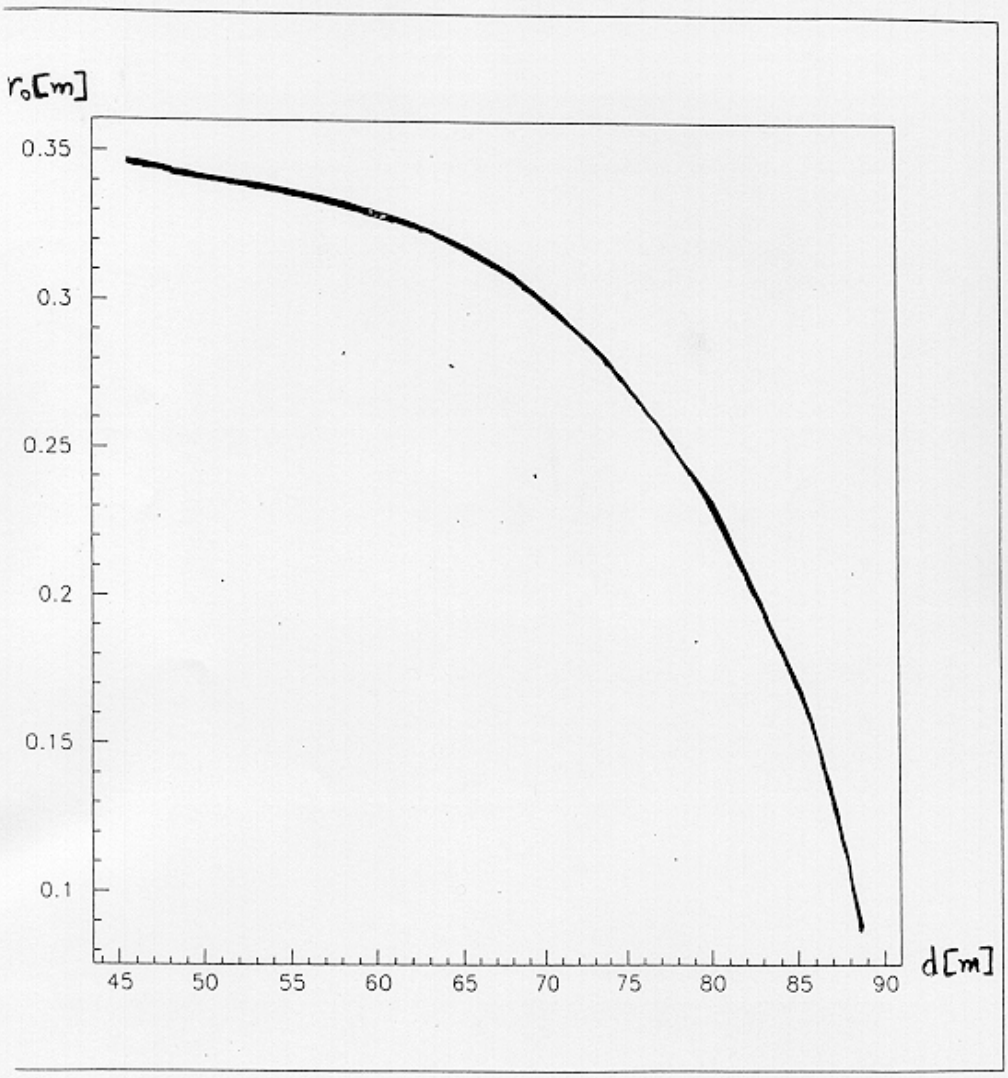

Reflector designed with parameters p = 100 GeV/c , D_R =90m and I_R =120kA.

Figure (4-4)

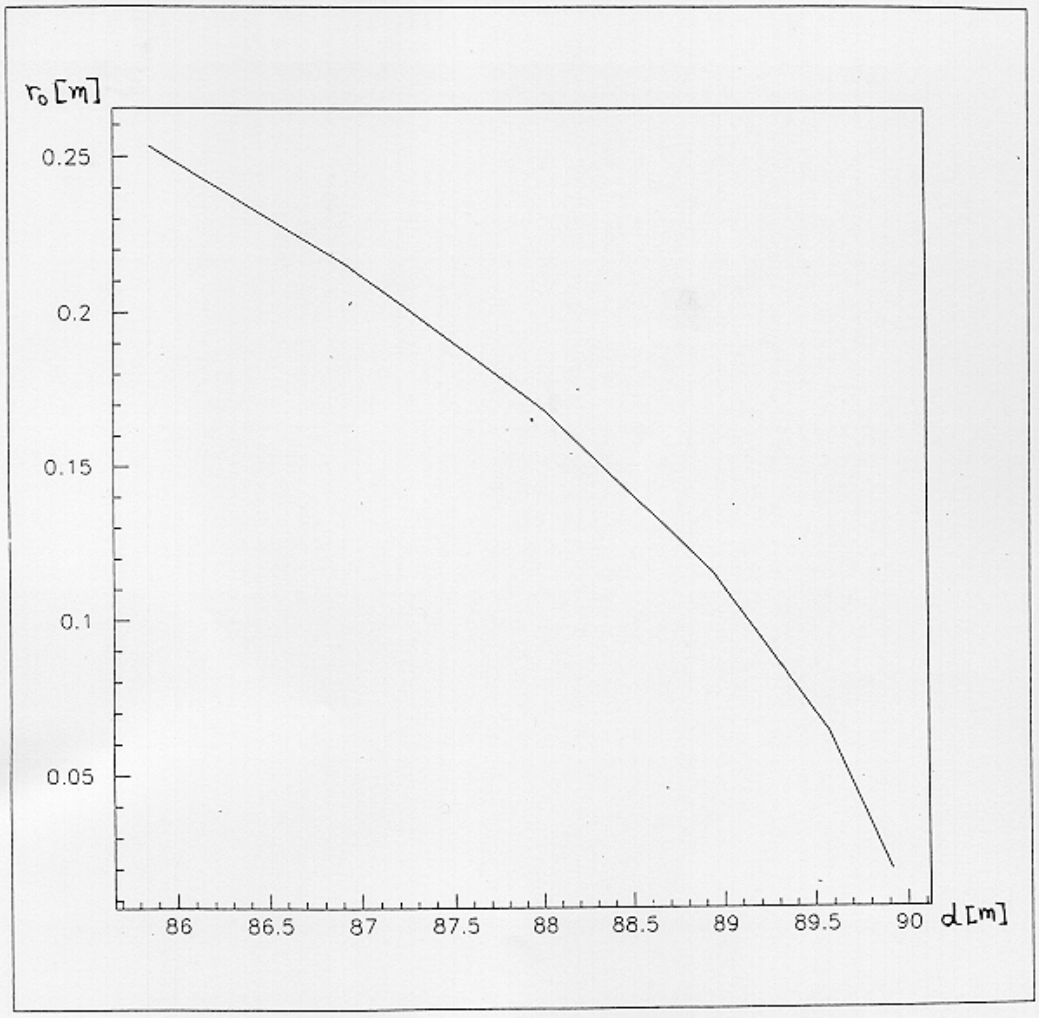

Reflector designed with parameters p = 20 GeV/c , D_R =90m and I_R =120kA.

CHAPTER 5
CONCLUSIONS

1. PRELIMINARY ATTEMPTS TO TAKE INTO ACCOUNT THE ACTUAL E AND p_T DISTRIBUTIONS OF THE NEUTRINO PARENT PARTICLES.

In the previous chapters the determination of the shape of the horn and reflector inner conductor was based on the assumption of isotropical production of neutrino parent particles (mainly π^+ and K^+) in the range of emission angles $\varphi \in$ [-10mrad,+10mrad] . Furthermore, the inner conductor was designed to perfectly focus a monoenergetic beam of particles in each case (horn or reflector). However, the neutrino parent particles of interest (π^+, K^+) are produced in the target with a vast energy distribution and a non-isotropical angular distribution for $\varphi \in$ [-10mrad,+10mrad] .

We used the Monte Carlo programs NUBEAM and FLUKA '95 which simulate the hadronic interactions of 450 GeV protons in the beryllium target and all other processes taking place along the WANF beam line. Assuming an intensity of 10^4 protons on target we had the energy (E in GeV) and the transverse momentum ($p_T \equiv p\,\varphi$ in GeV / c) distributions for secondary π^+ just after the target (no collimation assumed).These distributions are given respectively in figures (5-1) and (5-2).

Assuming a horn with parameters D_H = 20m and I_H = 120kA we calculated the point at which each π^+ of momentum $p \cong \frac{E}{c}$ and $\phi = \frac{p_T}{P}$ with E and p_T given by the distributions should enter the magnetic field of the horn.

In order to get a clear shape we had to put some cuts on the π^+ energy and emission angle, that is to select from the whole distribution only those π^+ for which

- $\varphi \leq$ 10mrad and
- (all momenta) or (p > 20 GeV/c) or (20 GeV/c < p < 60 GeV/c) .

The resulting inner conductor shapes are given in figures (5-3),(5-4) and (5-5) respectively.

The conclusion is that for a quite narrow range of the energy and the emission angle of the neutrino parent particles a reliable horn can be designed.

2.FINAL REMARKS.

In this study we started from first principles and our results can be applied to determine the shape of any horn or reflector inner conductor by merely choosing the parameters p, φ, D and I as it is required. The approximative formula (3-42) is very exact and can be used for a detailed preliminary design.

Furthermore, we need to compromise and match different horn and reflector pairs in order to choose the focusing pair which would maximize the parent particle flux at the end of the neutrino cave, leading to a maximum ν_μ flux in the detectors downstream.

Another vital problem is the choice of the collimation options for the target and matching them with the focusing system to find the most suitable combination. At this stage a total reconsideration of the horn-reflector pair might be necessary since the secondary particle yields will be affected by the presence of the collimator.

Figure (5-1) a

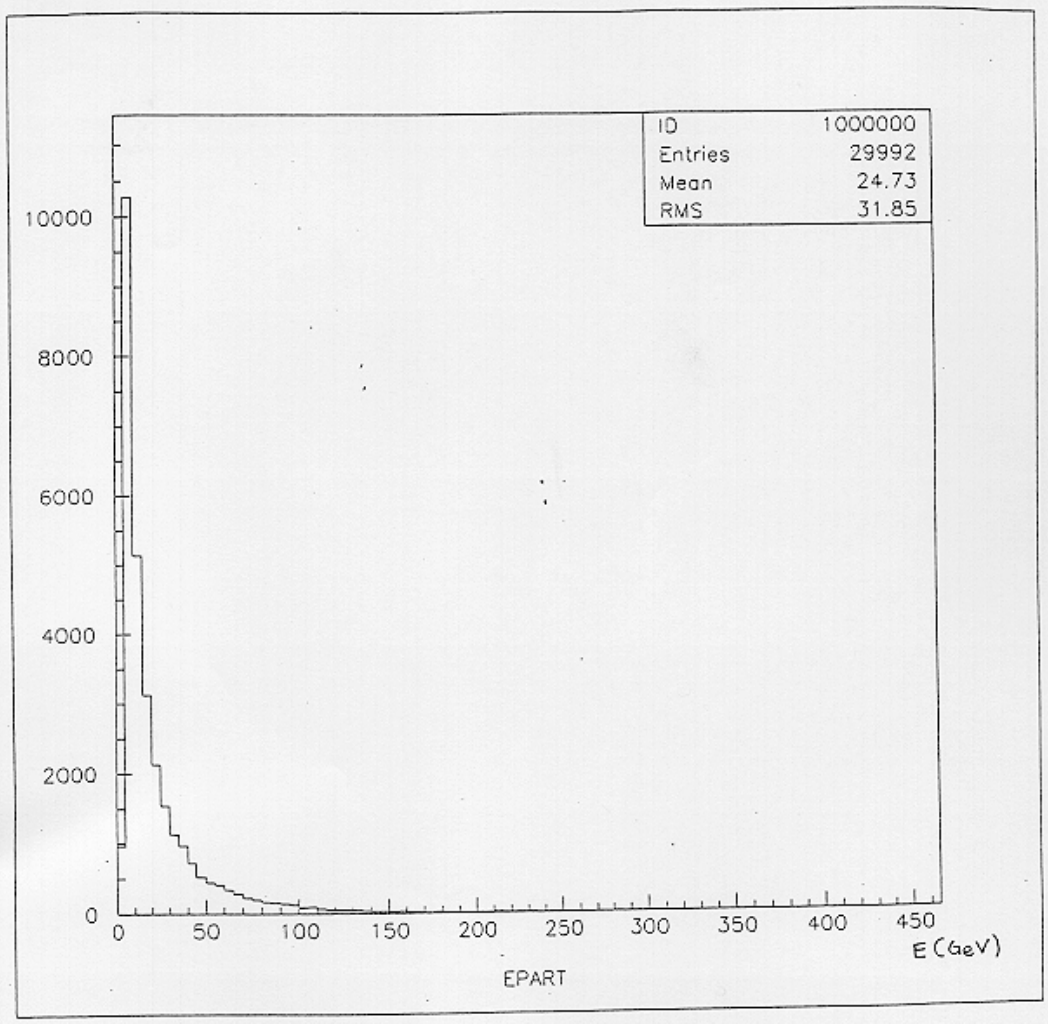

π^+ energy distribution just after the target.

Figure (5-1) b

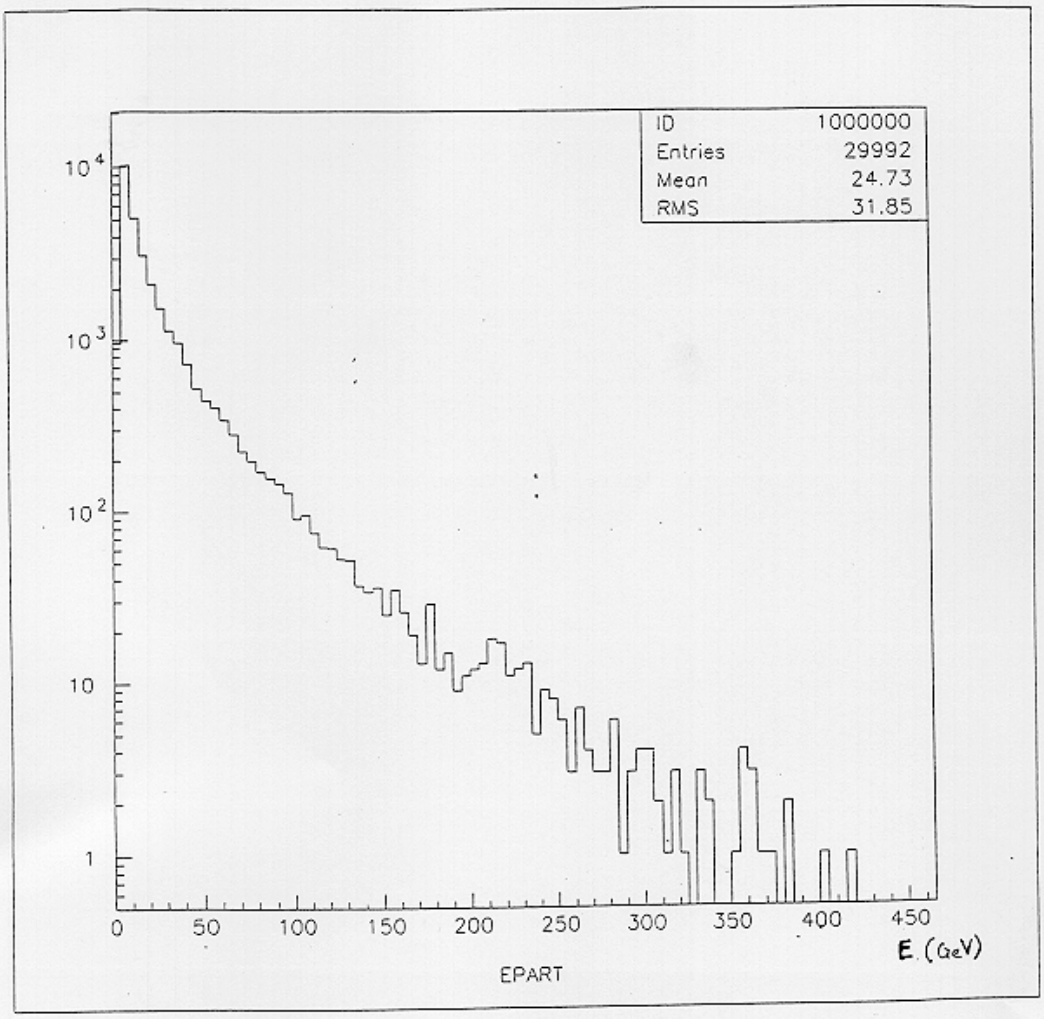

π^+ energy distribution just after the target.

Figure (5-2)

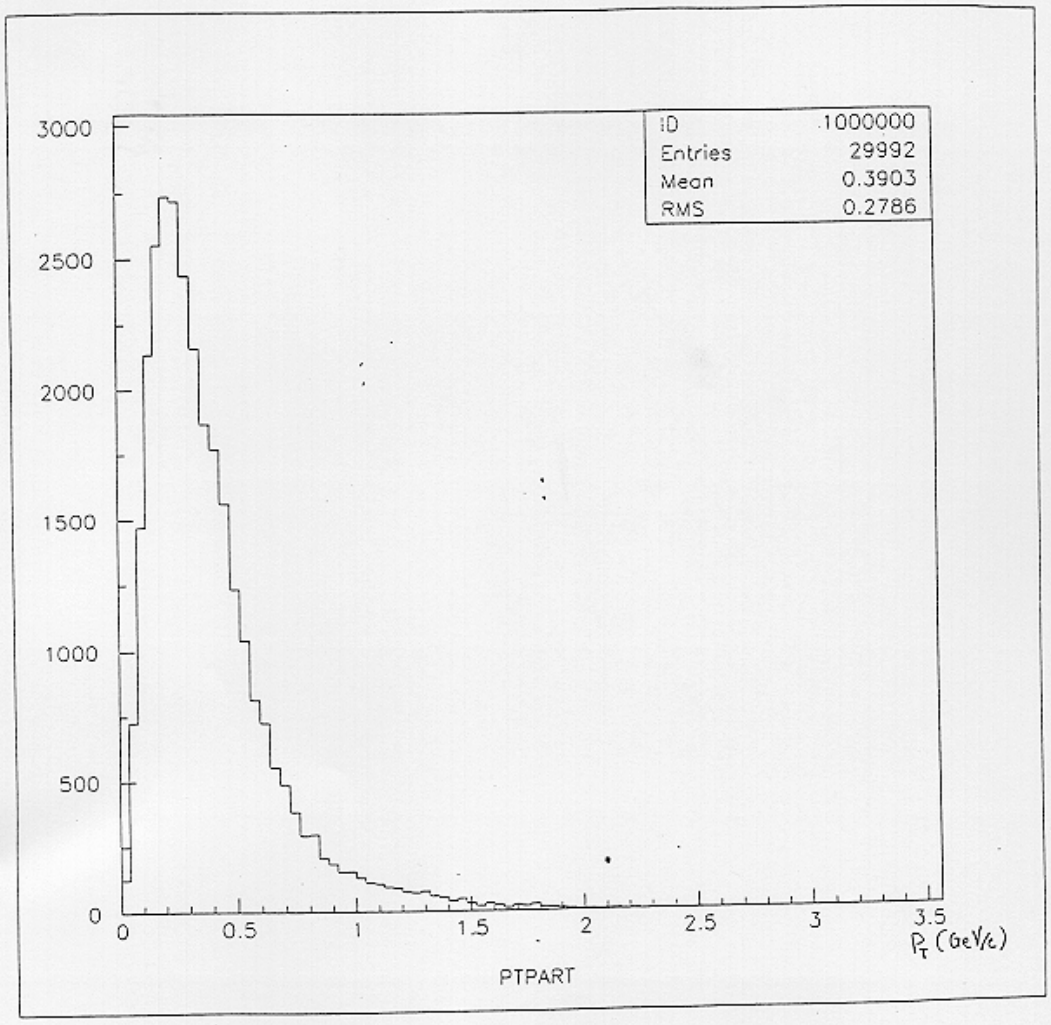

π^+ p_T distribution just after the target.

Figure (5-3) a

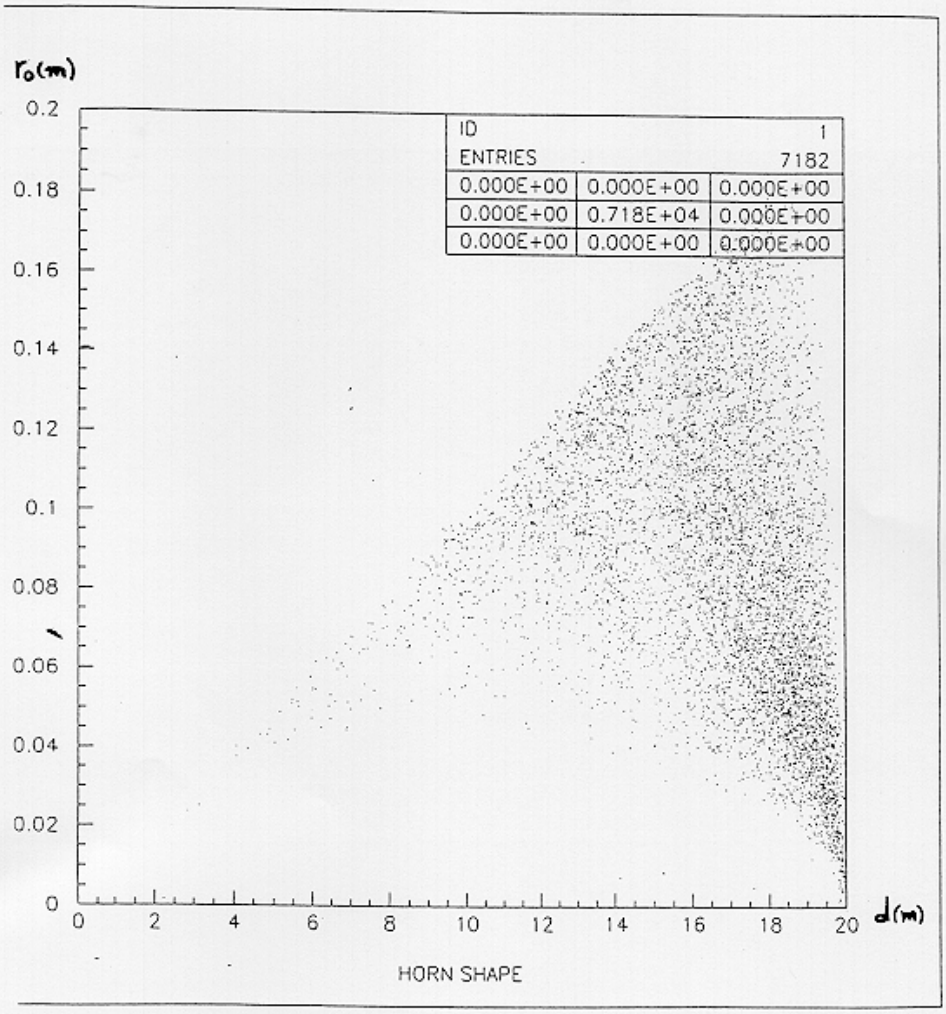

Horn designed for π^+ with $\varphi \leq 10$mrad and (all momenta).

Figure (5-3) b

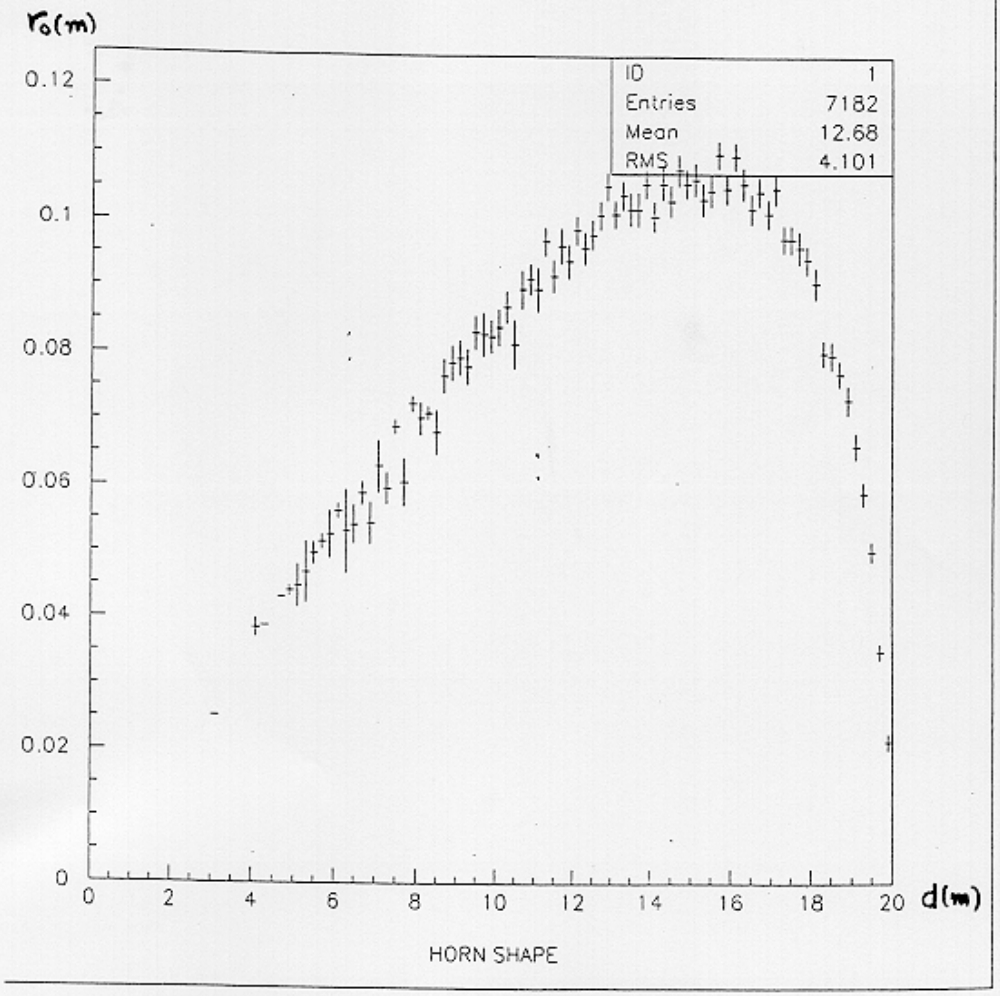

Horn designed for π^+ with $\varphi \leq 10$mrad and (all momenta).

Figure (5-4) a

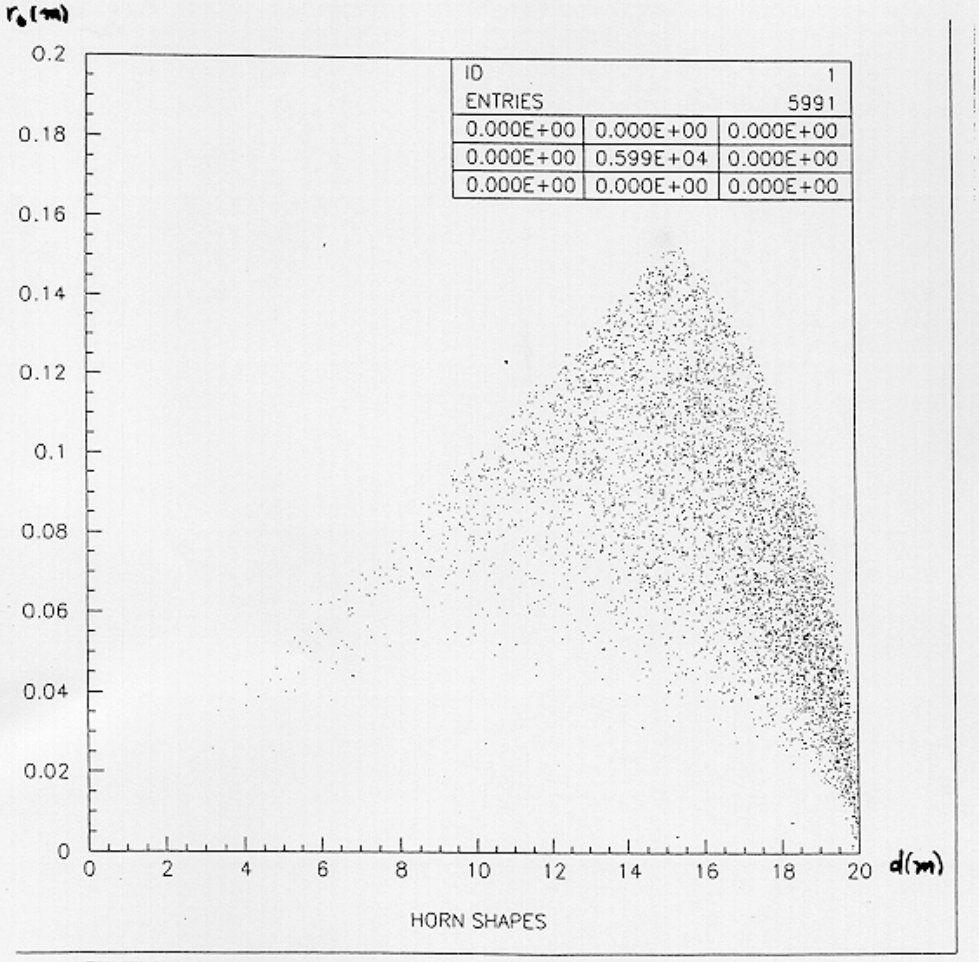

Horn designed for π^+ with $\varphi \leq 10$mrad and ($p > 20$ GeV/c).

Figure (5-4) b

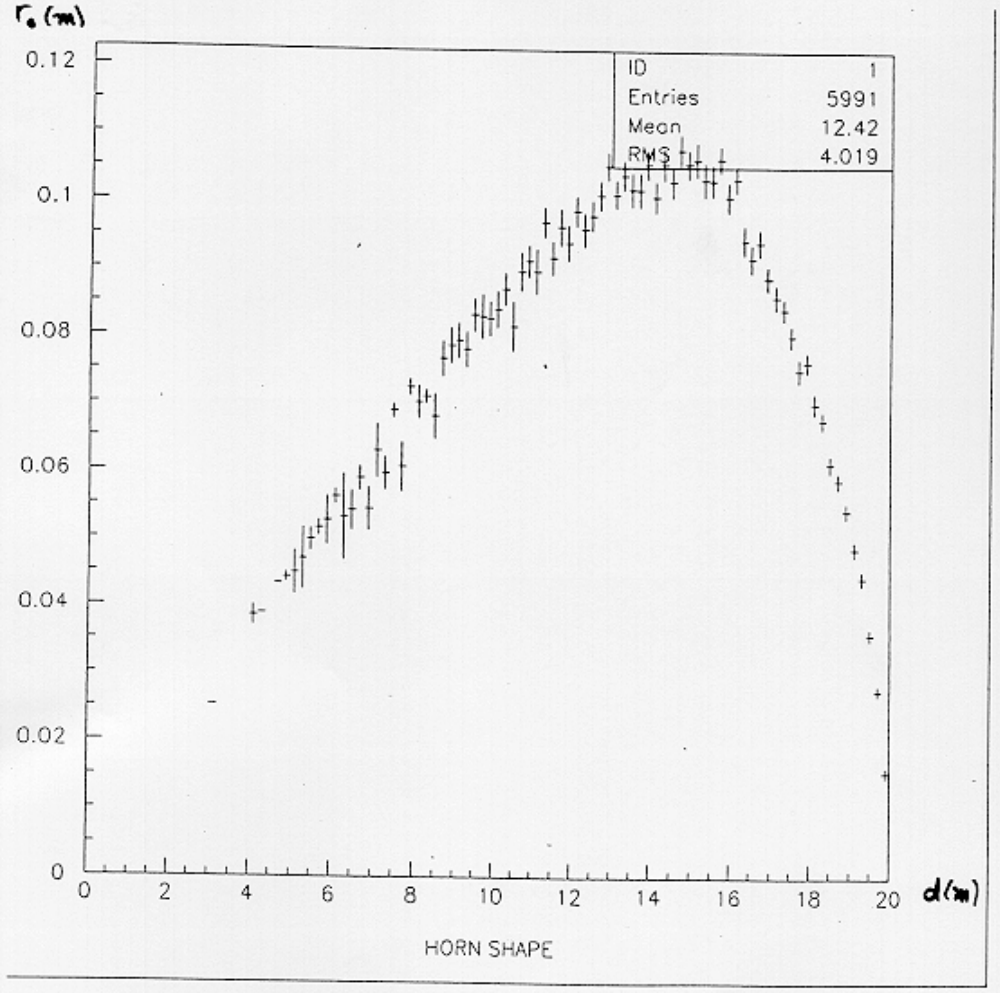

Horn designed for π^+ with $\varphi \leq 10$mrad and ($p > 20$ GeV/c).

Figure (5-5) a

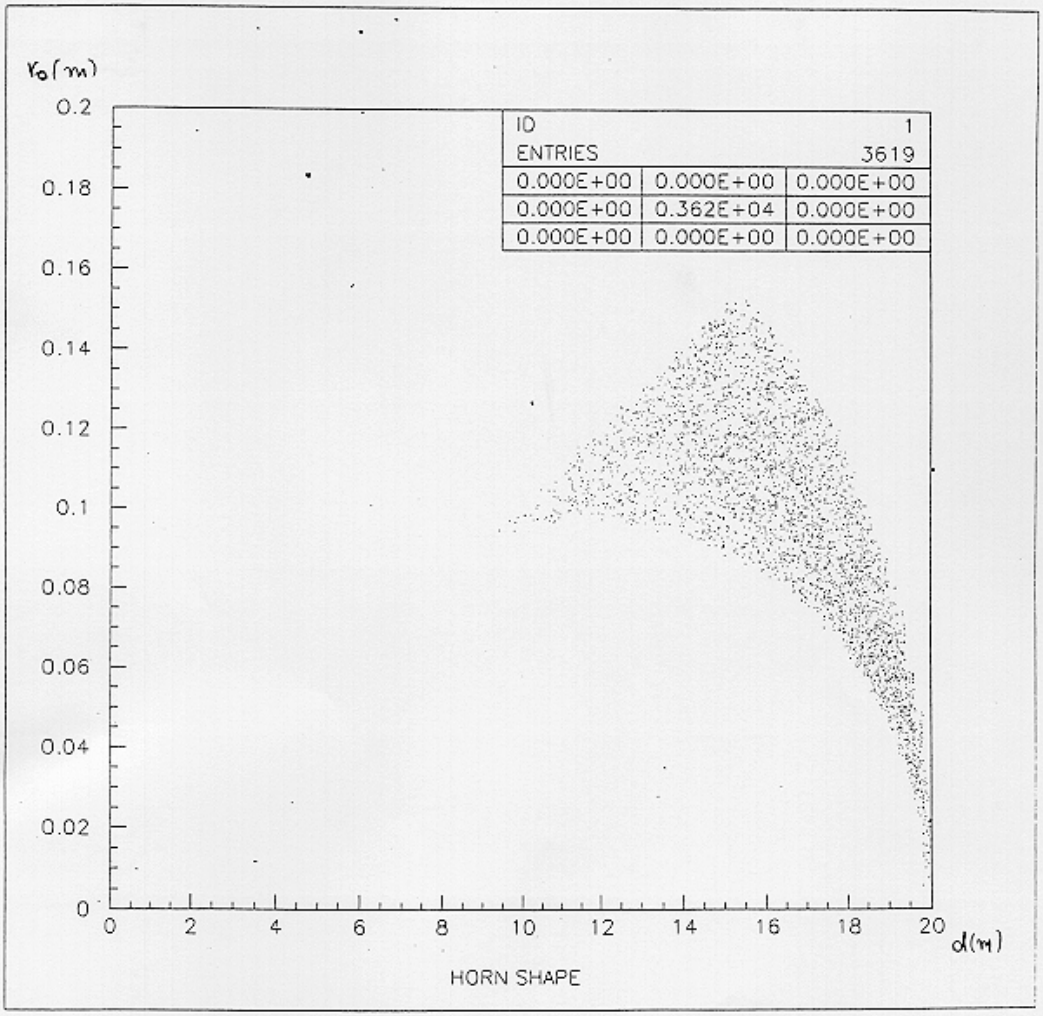

Horn designed for π^+ with $\varphi \leq 10$mrad and (20 GeV/c < p < 60 GeV/c).

Figure (5-5) b

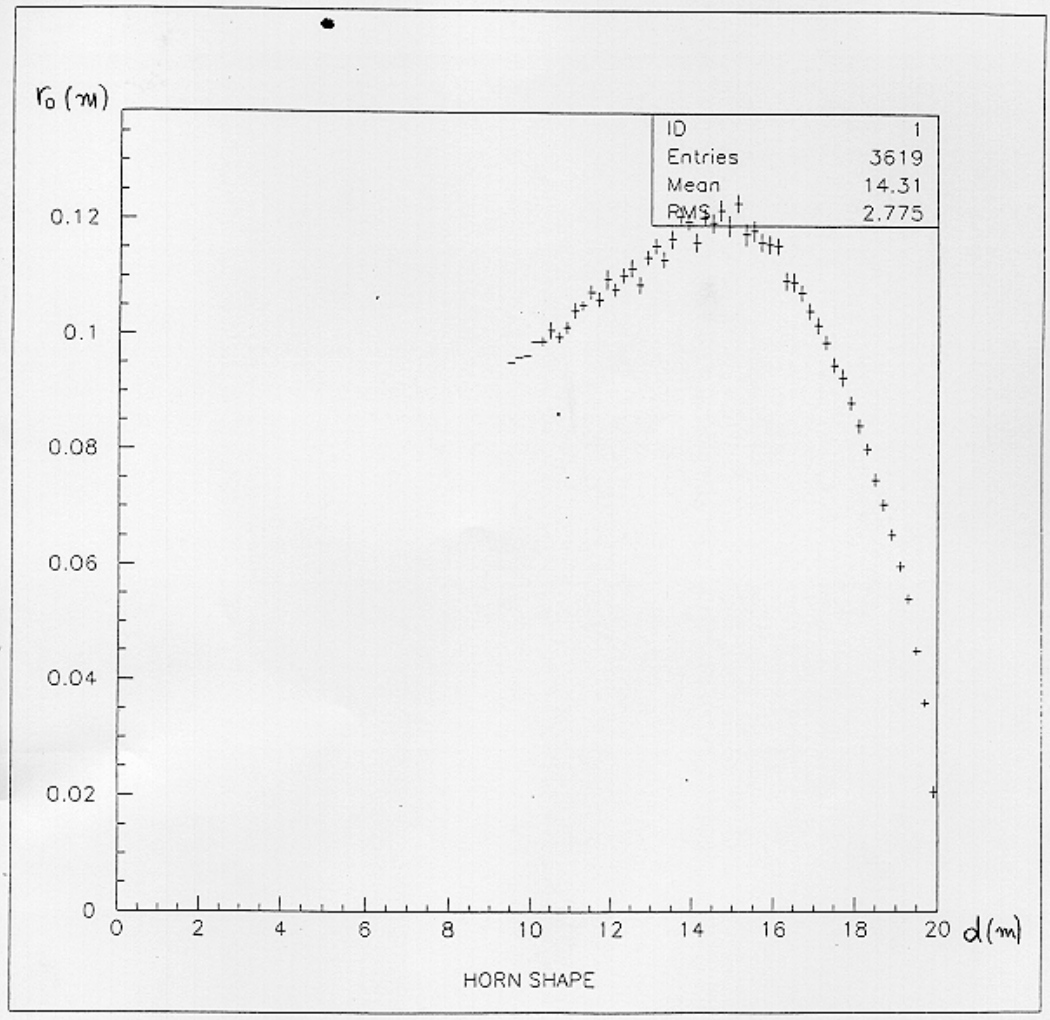

Horn designed for π^+ with $\varphi \leq 10$mrad and (20 GeV/c < p < 60 GeV/c).

LIST OF REFERENCES.

[1] S. Van der Meer, CERN 61-7

A directive device for charged particles and its use in an enhanced neutrino beam.

[2] S. Van der Meer, CERN 62-16

The beam guide, a device for the transport of charged particles.

[3] S. Van der Meer, CERN/PS/AA 80-12

Improved collection of secondaries from a long narrow target by a horn doublet.

[4] N.I Shtepa

Motion of a relativistic charged particle in the magnetic field produced by a constant cylindrical current of a rarified plasma.

[5] A.Ball

A blind man's guide to horn design.

[6] A.Ball, CERN/ECP 95-13

Design studies for a long base-line neutrino beam.

[7] CERN/ECP 95-14

The West Area Neutrino Facility for CHORUS and NOMAD experiments (94-97 operation).

[8] CERN/PPE 97-059

The NOMAD experiment at the CERN SPS.

[9] L.Di Lella, CERN 96-04

Neutrino oscillations. Proceedings of the 1995 European School of High Energy Physics.

[10] INFN/AE-98/05

The CERN Neutrino beam to Gran Sasso. Conceptual technical design.